Clim Dyn (2016) 47:2155–2175
DOI 10.1007/s00382-015-2956-8

Intraseasonal variability of air temperature over the mid-high latitude Eurasia in boreal winter

Shuangyan Yang[1,2] · **Tim Li**[1,2]

Received: 27 July 2015 / Accepted: 16 December 2015 / Published online: 4 January 2016

Abstract The intraseasonal oscillation (ISO) of air temperature over the mid- and high-latitude Eurasia in boreal winter was investigated by NCEP-NCAR reanalysis data. It is found that the intraseasonal temperature disturbances exhibit maximum variability near the surface in the region of 50°–75°N, 80°–120°E and they propagate southeastwards at average zonal and meridional phase speeds of 3.2 and 2.5 m s^{-1}, respectively. The low-level temperature signal is tightly coupled with upper-tropospheric height anomalies, and both propagate southeastward in a similar phase speed. A diagnosis of the temperature budget reveals that the southeastward propagation is primarily attributed to the advection of the temperature anomaly by the mean wind. A wave activity flux analysis indicates that the southeastward propagating wave train is likely a result of Rossby wave energy propagation. The source of the Rossby wave train appears at the high latitude Europe/Atlantic sector, where maximum wave activity flux convergence resides. During its southeastward journey, the ISO perturbation gains energy from the mean flow through both kinetic and potential energy conversions. A physics-based empirical model was constructed to predict the intraseasonal temperature anomaly over southeast China. The major predictability source is the southeastward-propagating ISO signal. The data for 1979–2003 were used as a training period to construct the empirical model. A 10-yr (2004–2013) independent forecast shows that the model attains a useful skill of up to 25 days.

Keywords Mid-high latitude intraseasonal temperature variability · Southeastward propagation · Extended-range forecast

✉ Tim Li
timli@hawaii.edu

[1] International Laboratory on Climate and Environment Change and Key Laboratory of Meteorological Disaster of Ministry of Education, Nanjing University of Information Science and Technology, Nanjing, China

[2] International Pacific Research Center, Department of Atmospheric Sciences, University of Hawaii at Manoa, Honolulu, HI 96822, USA

1 Introduction

Since Madden and Julian (1971, 1972) firstly discovered the tropical intraseasonal oscillation (ISO), a number of studies have demonstrated that the ISO exists not only over the tropics (Murakami 1980; Lau and Chan 1986; Wang and Rui 1990; Annamalai and Slingo 2001; Teng and Wang 2003; Li and Wang 2005; Wang et al. 2006), but also over mid- and high- latitude regions (Jeong et al. 2008; Yang et al. 2010; Kikuchi and Wang 2009; Wang et al. 2012, 2013). The ISO over the tropics (its major eastward-propagating component was called as the Madden–Julian Oscillation, MJO), has received a lot of attention in the past, including its preferred zonal planetary scale (Wang 1988; Li and Zhou 2009), its Rossby–Kelvin wave couplet horizontal structure (Hendon and Salby 1994; Wang and Li 1994; Li and Wang 1994; Kiladis and Wheeler 1995; Chatterjee and Goswami 2004; Zhang 2005), its tilting vertical moisture and wind profiles (Sperber 2003; Jiang et al. 2004), its season-dependent phase propagation (Wang and Rui 1990; Madden and Julian 1994; Matthews 2000; Yokoi and Satomura 2006; Jiang and Waliser 2008; Maloney 2009; Hsu and Li 2012), and its interannual variation (Slingo et al. 1999; Teng and Wang 2003; Kajikawa and Yasunari 2005; Shinoda and Han 2005; Lin and Li 2008; Wen et al. 2011; see Li 2014 for a review of dynamic mechanisms related to

these observed characteristics including plantary zonal scale selection, eastward and northward propagation, and ENSO-phase dependence of the ISO variability). It has been shown that the ISO has a profound influence on tropical cyclone formation (Maloney and Hartmann 2000; Hall et al. 2001; Fu et al. 2007; Chen et al. 2009; Cao et al. 2014; Xu et al. 2014) and propagation (Bi et al. 2015), monsoon onset and intensity (Zhang et al. 2002; Jiang et al. 2004; Lorenz and Hartmann 2006; Mao et al. 2010; He et al. 2011) and the triggering of ENSO (Kessler 2002; Lengaigne et al. 2004).

In comparison with the tropical ISO, mid- and high- latitude ISO received much less attention. Anderson and Rosen (1983) and Krishnamurti and Gadgil (1985) pointed out the existence of the mid-high latitude ISO. It was suggested that the mid-latitude ISO is independent of tropical forcing (Knutson and Weickmann 1987; Ghil and Mo 1991). One possible source of the mid-latitude ISO is local air–sea interaction in North Pacific (Wang et al. 2012). By conducting idealized atmospheric general circulation model experiments, Wang et al. (2013) found that the mid-latitude ISO is primarily caused by local processes and the tropical forcing accounts for 20 % of total intraseasonal variability in boreal summer. A case study showed that the extended-range drought and flood events over the mid-low reaches of Yangtze River were closely related to the mid-latitude ISO variability in boreal summer (Yang et al. 2013a). The propagation and circulation characteristics of the ISO over the mid-high latitude are distinctive from those in the tropics (Yang et al. 2013b).

Currently the most challenging issue facing the weather and climate community is the gap of forecast skill between the weather scale (less than 10 days) and the climate scale (monthly or seasonal). The predictability source of this extended range (10–30-day) lies in the atmospheric ISO over tropics and the mid-high latitude area. Motivated by this societal need, in this study we intend to investigate the temporal and spatial patterns of winter air temperature variability in intraseasonal timescale. We will focus on the Eurasia Continent, the most populated continent in the world. The main objective of the current study is to reveal the structure and evolution features of the intraseasonal variability of atmospheric temperature over the mid-high latitude Eurasia in boreal winter, and the causes of the southeastward propagation of the ISO signal (including both the low-level temperature signal and the corresponding upper-level geopotential height signal) from low-level and upper level dynamics perspective.

The remaining part of the paper is organized as follows. Datasets and methods used in this study are described in Sect. 2. The structure and evolution characteristics of the intraseasonal temperature anomaly over the mid-high latitude Eurasia in boreal winter are described in Sect. 3. In Sect. 4, the cause of the southeastward propagation of the low-level temperature anomaly through the surface temperature budget analysis is revealed. In Sect. 5, a propagation mechanism attributed to upper-level Rossby wave dynamics is discussed. In Sect. 6, a multi-variate lag-regression model is constructed for the extended-range (10–30-day) prediction of intraseasonal temperature anomaly over southeast China. Conclusions and discussions are given in the last section.

2 Data and method

2.1 Data

Daily reanalysis data between 1979 and 2014 with a horizontal resolution of 2.5° × 2.5° provided by the National Centers for Environment Prediction-National Center for Atmospheric Research (NCEP-NCAR) (Kalnay et al. 1996) are used in the present study. The variables include temperature T, geopotential height Z, zonal wind u, meridional wind v and vertical p-velocity ω at 12 pressure levels (1000, 925, 850, 700, 600, 500, 400, 300, 250, 200, 150, and 100 hPa). The temperature at $\sigma = 0.995$ level is also used to represent the surface temperature. Stream function ψ and relative vorticity ζ were calculated from u and v by $\zeta = \frac{\partial v}{\partial x} - \frac{\partial u}{\partial y} = \nabla^2\psi (\nabla^2 = \frac{\partial^2}{\partial x^2} + \frac{\partial^2}{\partial y^2})$. In addition, daily surface air temperature data, derived from National Meteorological Information Center of China Meteorological Administration, at 106 ground observational stations over southeast China are also used.

2.2 Temporal filtering and temperature budget diagnosis

Two steps are used to derive the intraseasonal signals. Firstly, the mean and first four harmonics of the seasonal cycle were removed from the raw data. Secondly, the so-derived anomaly fields are filtered by the Lanczos band-pass (10–60-day) filter (Duchon 1979). The ISO signals in boreal winter are extracted through the above procedure. Here the winter is defined as the time period from December 1 to March 31 (DJFM). A total of 35 winters from 1979/80 to 2013/14 (total $35 \times 121 = 4235$ days, with February 29th in leap years being removed) are analyzed. The effective degree of freedom is estimated based on Bretherton et al. (1999).

To examine the key processes contributing to the propagation of the intraseasonal temperature anomaly, the temperature budget at a given pressure level is diagnosed. The anomalous temperature tendency equation may be written as (Holton 1992):

$$\left(\frac{\partial T}{\partial t}\right)' = -\left(u\frac{\partial T}{\partial x}\right)' - \left(v\frac{\partial T}{\partial y}\right)' - \left(\omega\frac{\partial T}{\partial p}\right)' + \left(\omega\frac{\alpha}{C_p}\right)' + \left(\frac{\dot{Q}}{C_p}\right)' \quad (1)$$

where α is the specific volume of air; C_p is the specific heat of air, and $\dot{Q}$ denotes the rate of diabatic heating. The other symbols follow convention in meteorology.

Each of dependent variables may be separated into three components, an intraseasonal (10–60 days, denoted by a single prime), a synoptic-sale (<10 days, denoted by a double prime) and a low-frequency background state (LFBS, >60 days, denoted by an overbar) component. The LFBS and the synoptic-scale component are obtained by a low-pass (greater than 60 days) and a high-pass (less than 10 days) filter, respectively. Here the LFBS includes the annual cycle and other scale motion of greater than 60 days. After separating the three components, each advection term may be decomposed into nine terms. For example, the meridional temperature advection anomaly $-(v\frac{\partial T}{\partial y})'$ can be expressed as:

$$\begin{aligned}-\left(v\frac{\partial T}{\partial y}\right)' &= -\left[(\bar{v}+v'+v'')\frac{\partial(\bar{T}+T'+T'')}{\partial y}\right]' \\ &= -\left(\bar{v}\frac{\partial \bar{T}}{\partial y}\right)' - \left(\bar{v}\frac{\partial T'}{\partial y}\right)' - \left(\bar{v}\frac{\partial T''}{\partial y}\right)' \\ &\quad - \left(v'\frac{\partial \bar{T}}{\partial y}\right)' - \left(v'\frac{\partial T'}{\partial y}\right)' - \left(v'\frac{\partial T''}{\partial y}\right)' \\ &\quad - \left(v''\frac{\partial \bar{T}}{\partial y}\right)' - \left(v''\frac{\partial T'}{\partial y}\right)' - \left(v''\frac{\partial T''}{\partial y}\right)' \quad (2)\end{aligned}$$

2.3 Energy conversion and wave-activity flux

The barotropic energy conversion was originally derived by Simmons et al. (1983) and Mak and Cai (1989), in which the time-mean winds are assumed to be non-divergent. Considering that the wind in the current study involves both rotational and divergent components, we apply the barotropic energy conversion equation derived by Maloney and Hartmann (2001). The barotropic kinetic energy conversion between the winter mean flow and the ISO flow can be written as:

$$\overline{\overline{CK}}_{iso} = -\overline{\overline{u'^2}}\frac{\partial \bar{\bar{u}}}{\partial x} - \overline{\overline{v'^2}}\frac{\partial \bar{\bar{v}}}{\partial y} - \overline{\overline{u'v'}}\frac{\partial \bar{\bar{u}}}{\partial y} - \overline{\overline{u'v'}}\frac{\partial \bar{\bar{v}}}{\partial x} \quad (3)$$

where a single prime denotes intraseasonal perturbation as stated above, and a double overbar denotes the winter time mean. A positive (negative) value of $\overline{\overline{CK}}_{iso}$ indicates that the ISO flow gains (loses) kinetic energy from (to) the mean flow.

In addition, the potential energy conversion between the ISO and the mean flow is also diagnosed. The mean and perturbation potential energy equations can be derived from the thermodynamic equation (Holton 1992). By multiplying temperature in the thermodynamic equation, both time-mean and perturbation potential energy equations can be derived. The common term in the two equations representing potential energy conversion between the mean flow and the perturbation flow can be expressed as:

$$\overline{\overline{CP}}_{iso} = -\frac{g}{(\gamma_d-\gamma)T_0}\left(\overline{\overline{u'T'}}\frac{\partial \bar{\bar{T}}}{\partial x} + \overline{\overline{v'T'}}\frac{\partial \bar{\bar{T}}}{\partial y}\right) \quad (4)$$

where g is the gravity, $T_0 = 288.15$ K representing the standard sea level temperature, γ_d and γ are the dry adiabatic lapse rate and the actual lapse rate of atmosphere, respectively. Here $\gamma_d - \gamma$ is set to be 4.0×10^{-3} °C m^{-1}. A positive (negative) value of $\overline{\overline{CP}}_{iso}$ indicates that the ISO gains (loses) potential energy from (to) the mean flow. Equation (4) implies that the conversion between the mean potential energy and perturbation potential energy is determined by horizontal eddy heat fluxes and mean thermal gradients.

A phase-independent wave-activity flux (WAF) formulated by Takaya and Nakamura (2001) is used to investigate Rossby wave energy propagation and accumulation. This wave flux formulation has been used in the study of Pacific easterly waves (e.g., Tam and Li 2006) and midlatitude ISO (e.g., Zhao et al. 2013; Wang et al. 2013). A two dimensional WAF may be expressed as:

$$W = \frac{1}{2|\bar{U}|}\begin{bmatrix}\bar{u}\left(\psi_x'^2 - \psi'\psi'_{xx}\right) + \bar{v}\left(\psi'_x\psi'_y - \psi'\psi'_{xy}\right) \\ \bar{u}\left(\psi'_x\psi'_y - \psi'\psi'_{xy}\right) + \bar{v}\left(\psi_y'^2 - \psi'\psi'_{yy}\right)\end{bmatrix} \quad (5)$$

In Eq. (5), the subscript indicates partial derivative; ψ denotes the stream function; $\boldsymbol{U} = (u, v)^{Tr}$ is wind velocity (superscript T_r denotes vector transpose).

2.4 A non-filtering method and a multi-variate regression model

The real-time prediction of intraseasonal temperature variability requires us to extract the ISO signals from the raw data without band-pass filtering. To construct an empirical model for real-time forecast, a non-filtering method developed by Hsu et al. (2015) is applied. This non-filtering method consists of the following three steps. Firstly, a daily climatologic annual cycle field is removed from the raw data. The so-derived dataset is called "Var$_1$". Secondly, the lower-frequency signals with the period longer than 60 days are removed from Var$_1$. This is done by subtracting the previous 30-day running mean (i.e., from day −30 to day 0). The so-derived dataset is called "Var$_2$". Finally, the dataset Var$_2$ is subject to a previous 5-day running mean (i.e., from day −5 to day 0) to remove the higher-frequency synoptic-scale component (10 days or less). The final dataset is considered to represent the 10–60-day intraseasonal component.

Once the ISO signals are extracted, we further use the dataset to construct a multivariate lag-regression (MVR) empirical model (Jones et al. 2004; Hsu et al. 2015). In

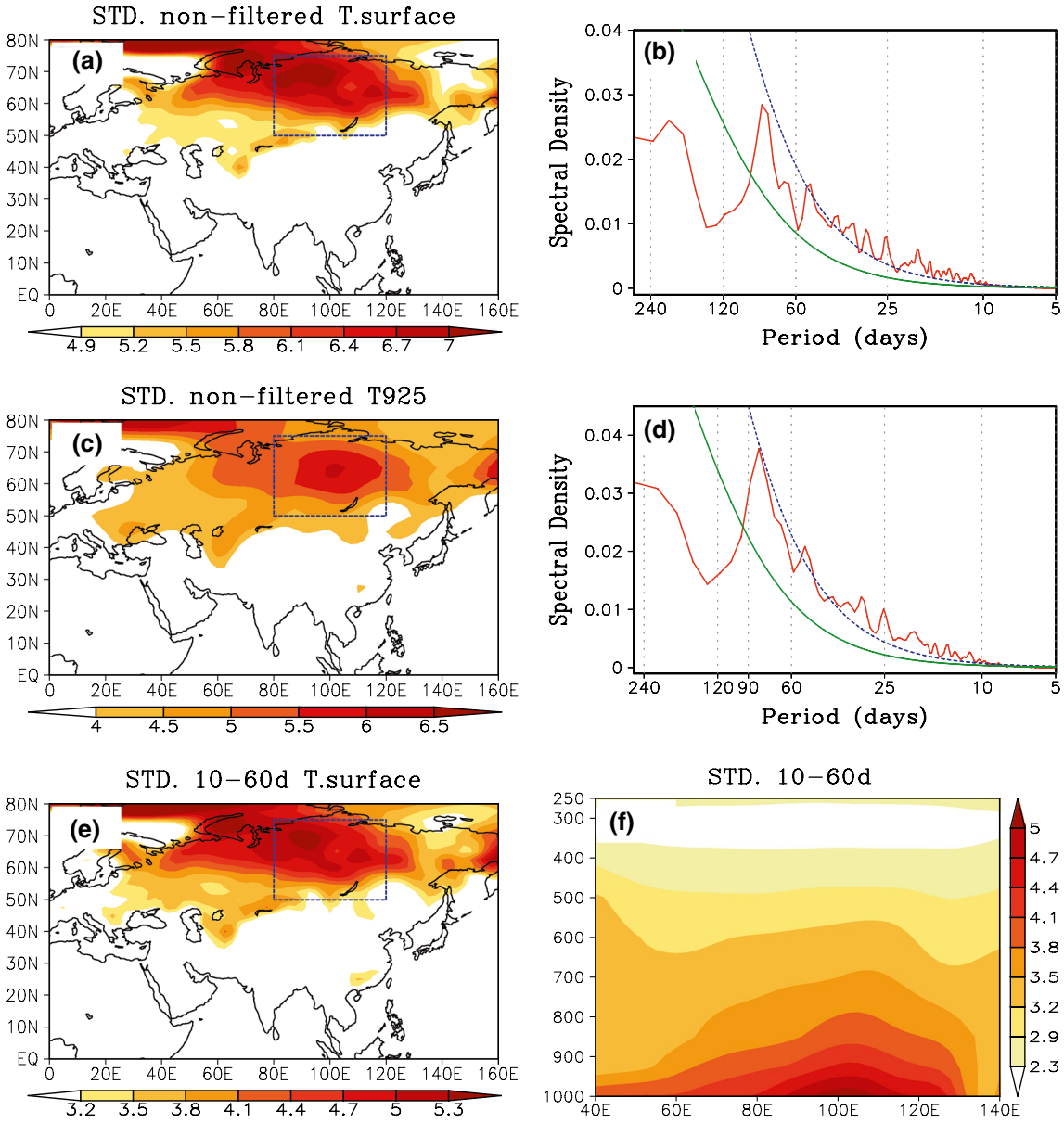

Fig. 1 **a** Standard deviation of non-filtered surface temperature anomalies (unit: K; with the mean and first four harmonics of the seasonal cycle and the high-frequency component removed) in boreal winter (December–March, DJFM). The *box* denotes the activity center of temperature anomalies. **b** Power spectral analysis of non-filtered surface temperature anomalies averaged in the *box area* in (**a**). The *green* and *red lines* denote spectrum density of red noise and its 0.01 significance level, respectively. **c**, **d** As in (**a**, **b**) respectively, but for 925 hPa. **e** As in (**a**), but for 10–60-day filtered surface temperature anomalies. **f** Zonal-vertical distribution of standard deviation of 10–60-day filtered temperature anomalies along 60°N

such a model, predictand Y is determined by multivariate linear regression of the preceding values of a series of predictors X. The MVR model can be expressed as:

$$Y = \sum_i a_i X_i(t) + \varepsilon_{t+n} \tag{6}$$

where t is time; n denotes forecast lead; a_i is the regression coefficient determined by least square estimation; X_i are predictors; and ε_{t+n} represents a random component.

3 Structure and propagation characteristics of the intraseasonal temperature anomaly

Figure 1a shows the standard deviation (STD) of non-filtered surface temperature anomalies over Eurasia Continent. Note that the maximum perturbation center is located at the mid-high latitude region around 50°–75°N, 80°–120°E (marked by a rectangle). The same activity centers are found at 925 hPa (Fig. 1c) and upper level

with reduced amplitude (not shown). The non-filtered temperature anomalies above are obtained by removing the mean and first four harmonics of the climatologic annual cycle firstly, and then conducting a 5-day running mean to remove the higher-frequency synoptic-scale component.

An area-averaged (50°–75°N, 80°–120°E) temperature anomaly is then subject to a power spectrum analysis. It is found that the statistically significant signal of the temperature anomalies at surface (Fig. 1b) and 925 hPa (Fig. 1d) appears at a period of 10–60 days. It is worth mentioning that the intraseasonal signal is still statistically significant even if one keeps the synoptic component. The same power spectrum peak is also found in this period range in the upper tropospheric geopotential height field (not shown). Thus, in the rest of this paper, we will primarily focus on the 10–60-day period band, unless indicated otherwise.

Figure 1e illustrates the STD of 10–60-day filtered surface temperature anomalies in the same region. Again the maximum activity center is located in the region of 50°–75°N, 80°–120°E. The intraseasonal temperature variability explains about 25 % of total variability (including the annual cycle and the interannual, intraseasonal, and synoptic components). The temperature signal is greatest at the surface, and decays with height in the troposphere as shown from the zonal-vertical distribution of the STD of 10–60-day temperature anomalies along 60°N (Fig. 1f).

To reveal the dominant patterns of the intraseasonal temperature anomalies over the mid-high latitude Eurasia in boreal winter, an empirical orthogonal function (EOF) analysis is performed on the 10–60-day surface air temperature anomalies in the domain of 35°–80°N, 20°–140°E (931 points in space) for winters from 1979/80 to 2013/14. The horizontal patterns of the first mode (EOF1) and the second mode (EOF2) and the time-lag correlation coefficient between the first two principal components (PC1 and PC2) are depicted in Fig. 2. Note that the variance contributions of EOF1 and EOF2 are 18.5 and 16.1 %, respectively. The first two leading modes are statistically independent from higher modes based on the estimation of error range of eigenvalues proposed by North et al. (1982). Figure 2a, b show that two positive temperature perturbation centers are located at 65°N and 55°N respectively. The significant lagged correlation between PC1 and PC2 in Fig. 2c suggests that PC1 leads PC2 by 4 days and that the two leading modes reflect the same propagating mode at different phases.

To clearly describe the evolution of the intraseasonal temperature signal, we conduct a composite analysis. Strong and weak cases are selected based on PC1 time series. The criterion for strong negative (positive) events is that standardized PC1 exceeds −1.5 (+1.5). Total 69 strong negative and 63 strong positive events are selected for the composite analysis.

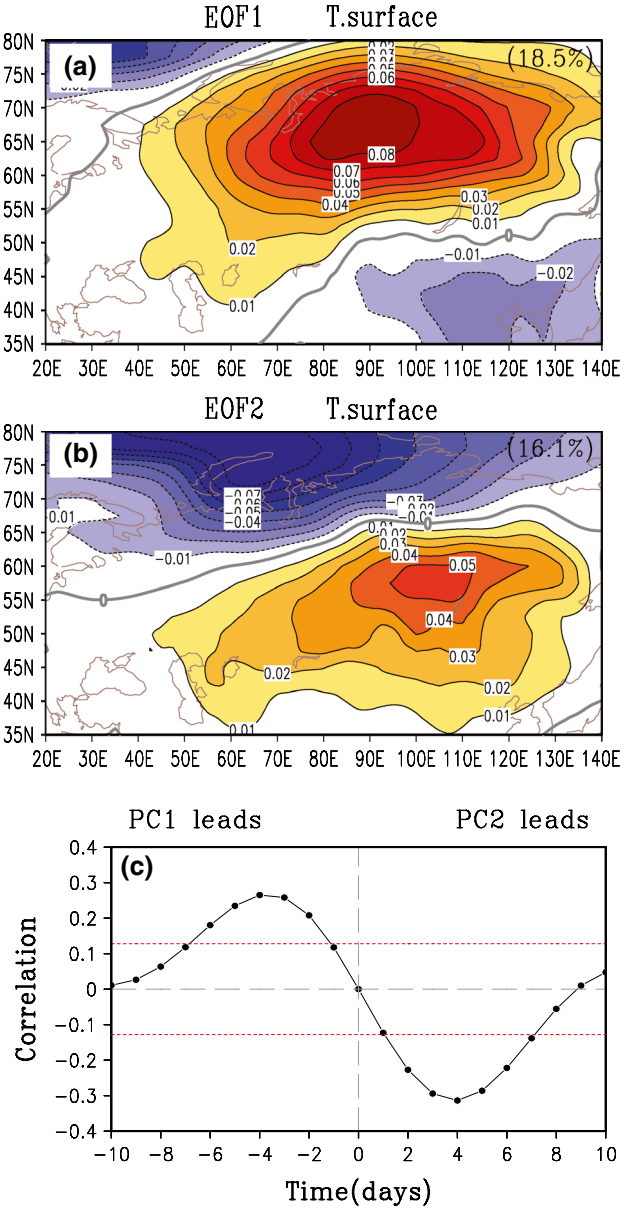

Fig. 2 **a** The EOF1 pattern of the 10–60-day filtered surface temperature anomalies in DJFM (values larger and less than 0.01 are *shaded*; *yellow*: positive; *blue*: negative; *thick gray lines* denote zero contours, as follows). The variance contribution is marked at the *upper-right corner*. **b** As in (**a**), but for the EOF2. **c** The lead-lag correlation coefficients between PC1 and PC2. The *red dash lines* denote the 0.05 significant level; positive (negative) days mean PC2 leads (lags) PC1

The evolution of composite 10–60-day surface temperature anomalies from day −8 to day +10, at an interval of 2 days, is portrayed in Fig. 3. Because the positive event composite is approximately a mirror image of the negative events, what we plotted here is the difference between the strong positive and the strong negative ISO events. Day 0 represents the time when the positive center of surface

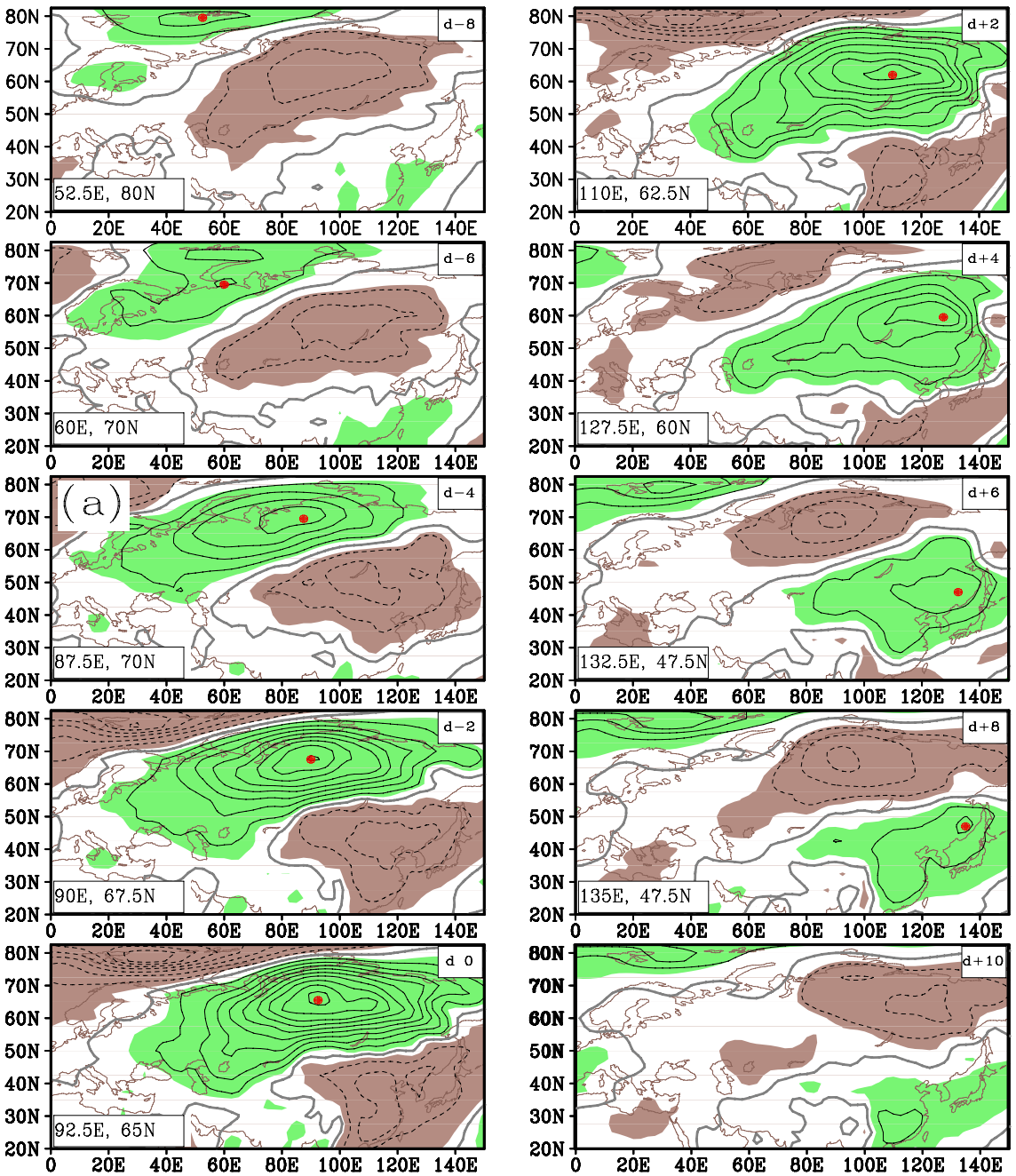

Fig. 3 Evolution of the composite 10–60-day surface temperature anomalies (contours with an interval of 2 K) from days −8 to +10, with an interval of 2 days. The day numbers are drawn at the *upper right-hand corner* of the appropriate panel. *Green* (*brown*) *shading* area indicates the positive (negative) area exceeding 0.05 significance level. The *red dots* represent the centers of the maximum positive surface temperature anomalies associated with the southeastward propagation; the latitudinal and longitudinal values of the dots are written at the *lower left-hand corner*

temperature anomalies appears at the same location as shown in EOF1 structure (Fig. 2a). The composite maps clearly illustrate the southeastward propagation of the temperature anomaly, as seen by the locations of the red dots representing the centers of the maximum positive temperature anomalies.

To quantitatively measure the propagation speed and direction, we calculate the propagation vector based on a local lagged correlation method developed by Lau and Lau (1990). For a given grid, the surface temperature anomaly at this grid point is regarded as a reference time series (35 boreal winters from 1979/80 to 2013/14). A lead-lag

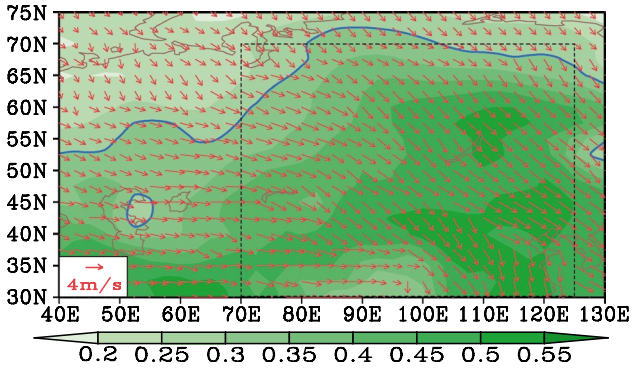

Fig. 4 Phase propagation vectors (*arrows*; unit: m s^{-1}; see scale at the *lower left corner*) and the temporal coherence (*shading*; see *scale bar*) of the composite 10–60-day surface temperature anomalies. The *blue lines* denote 0.3 contours of temporal coherence. The *box* indicates the area of 30°–70°N, 70°–125°E (where the coherence generally larger than 0.3). The temporal coherence means the average of the strongest positive lagged-correlation coefficients at day −5 and day +5, and see text for details of analysis procedure

correlation is calculated between time series of each surrounding grid points and the time series at the base point, from lagged day −5 to day +5. The direction of the phase propagation vector at a base-point is then inferred from the orientation of the line segment pointing from the strongest positive correlation center at day −5 to that at day +5. The magnitude of the propagation speed is estimated by dividing the distance of the line segment by the time interval (i.e., 10 days).

Figure 4 displays the so calculated phase propagation vectors and temporal coherence map (shading) for the 10–60-day surface temperature anomalies. Here the temporal coherence at a base-point is defined as the average of the strongest positive lagged correlation coefficients at day −5 and day +5. For example, for a series of lag-correlation charts corresponding to the common base point (called P), the strongest positive correlation point appearing at day −5 is identified (called A), and the strongest positive correlation point appearing at day +5 is also identified (called B). The temporal coherence of the migratory signal for the base point P is defined as the average of the lagged correlation coefficients at point A and point B. The temporal coherence describes how well a migratory signal is maintained through its evolution in time. The details of temporal coherence definition can be referred to Lau and Lau (1990). The arrows in Fig. 4 generally point southeastward, implying that the intraseasonal temperature signal propagates toward the south and east in northern winter. Taking the autocorrelation into account (Bretherton et al. 1999), the effective degree of freedom for the data we analyzed is about 244. A high temporal coherence is defined when its value exceeds 0.001 significance level (~0.21 for N = 244). Based on the above estimation,

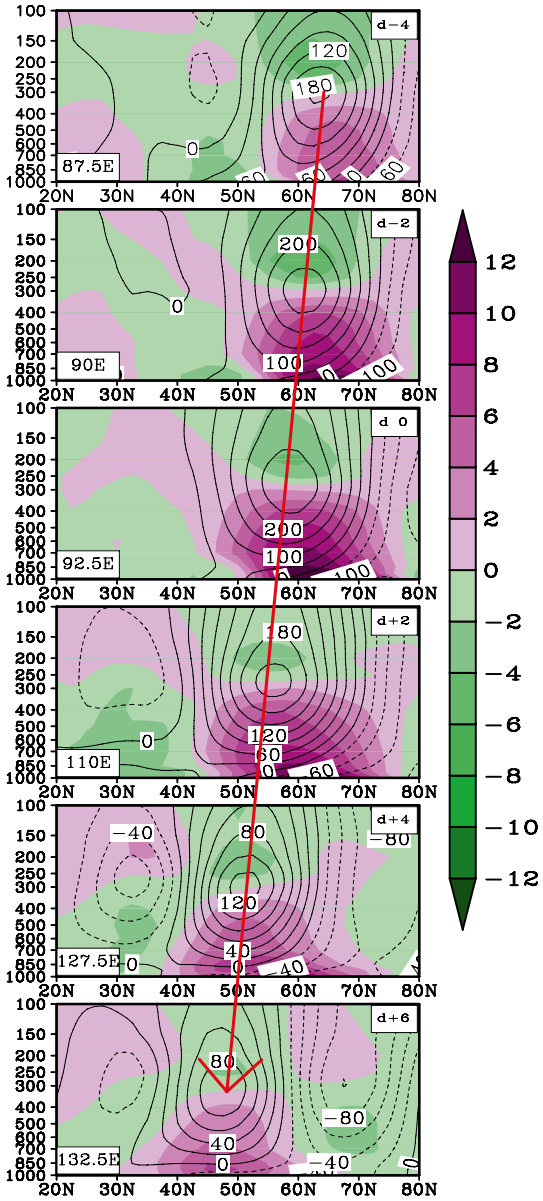

Fig. 5 The meridional-vertical distribution of composite 10–60-day filtered geopotential height Z' (contour; unit: gpm) and temperature T' (*shading*; unit: K) along the longitudes (written at the *lower left-hand* corner of the appropriate panel) of centers of the maximum positive temperature (see the *red dots* in Fig. 3) from day −4 to day +6

a value of 0.3 is used as a criterion for strong coherence. As shown, the contour of 0.3 covers most of the mid-latitude Eurasia, implying that the temperature propagation signal is of high temporal coherence in the region. Taking the area of 30°–70°N, 70°–125°E (the box in Fig. 4) as a key activity region (where the coherence is in general larger than 0.3), the average meridional and zonal phase speeds in the region are 2.5 and 3.2 m s^{-1}, respectively. Actual phase speeds may vary slightly with latitude and longitude.

Not only the low-level temperature signals but also the upper-level geopotential height anomalies show similar southeastward movement, which can be seen from either the temporal sequence of horizontal patterns of the temperature and geopotential height fields or their vertical cross sections. Figure 5 shows the meridional-vertical distributions of composite geopotential height Z' and temperature T' along the longitude position of the maximum surface T' center (i.e., the red dots in Fig. 3). At day −4, a positive Z' center at 300 hPa is located north of 60°N, and below (above) this center, the T' shows a warm (cold) anomaly, following well the hydrostatic relationship. At day +6, the positive Z' center moves southeastward to south of 50°N. The observational result above indicates that the low-level intraseasonal temperature signal is closely coupled with upper-tropospheric height anomalies through a hydrostatic relationship.

A clearer southeastward propagation of the geopotential height anomalies can be seen from the temporal evolutions of horizontal patterns of the intraseasonal height fields. Figure 6a shows the evolutions of composite Z' patterns at 300 hPa, where maximum Z' anomaly appears. Same as the low-level temperature perturbation, Z' at 300 hPa from day –4 to day +6 exhibits a clear southeastward propagation. The average phase speed and direction are quite similar to those of the surface temperature anomalies, as inferred from the evolution of the positive Z' centers (i.e., the red dots in Fig. 6). A similar propagating feature also appears in the Z' field at 600 hPa (Fig. 6b), implying that the southeastward wave train has an equivalent barotropic vertical structure. In fact, the composite relative vorticity anomalies ζ' and stream function anomalies ψ' show similar vertical structures.

To investigate to what extent the local intraseasonal temperature variability is connected to large-scale circulation patterns, we conducted singular value decomposition (SVD) analysis. The SVD analysis can effectively derive coupled mode variability between two fields (called left field and right field) (Bretherton et al. 1992). There are a number of key parameters in the SVD analysis. The first, which is called the squared covariance fraction (SCF), denotes the contribution of each SVD mode to the total covariance between left field and right field. The second important parameter, which is termed as the variance fraction (VF), measures the contribution of a derived SVD mode to the total variance of each individual field (Bretherton et al. 1992; Wang et al. 2003). We select the intraseasonal surface temperature anomalies over the area of 50°–75°N, 80°–120°E (where the maximum temperature perturbation center is located) as the left field, and the intraseasonal geopotential height anomalies over Eurasia at 300 hPa (at which level the maximum height perturbation is located) as the right field. The accumulated SCF of the first two pairs of SVD modes is 91 %. The total VF of the left field is 65 %, implying that the intraseasonal temperature anomalies associated with the Eurasian geopotential height anomalies accounts for 65 % of the total intraseasonal variances of the temperature anomalies.

4 Cause of the southeastward propagation: a surface temperature budget analysis

The observational analysis above indicates that both the low-level temperature and upper-level height anomalies show a coherent southeastward propagation characteristic. To understand the mechanism responsible for the southeastward propagation of the intraseasonal temperature anomaly, we conduct a vertically integrated temperature budget analysis. Our strategy is to examine the contributions of each term in the right hand side of the thermodynamic Eq. (1) to the local temperature change rate $\partial T'/\partial t$ at day 0. Note that because the apparent heat source term (i.e., the diabatic heating term) was diagnosed from the temperature equation with the original daily reanalysis data according to Yanai et al. (1973), the temperature budget above is exactly in balance. As shown in Fig. 5, the sign of the temperature anomaly at low level is opposite to that at upper level (above 300 hPa), so we conduct temperature budget analyses at low level and upper level respectively. For low level, we diagnosed the 925–500 hPa integrated temperature budget (1000 hPa is excluded simply because this pressure level is not always above the surface of the earth). A similar result is derived for 1000–500 hPa integrated temperature budget in the region where 1000 hPa is above the surface. For upper level, we diagnosed the 200–150 hPa integrated temperature budget (where major opposite temperature signals appear). The reason we use multiple levels rather than a single level for the budget diagnosis is to obtain a statistically significant, more robust result.

Figure 7a depicts vertically integrated (925–500 hPa) T' and $\partial T'/\partial t$ patterns at day 0. As shown, a positive $\partial T'/\partial t$ center appears to the southeast of a positive T' center. Because of this positive tendency, the temperature perturbation moves further southeastward. To investigate the cause of the positive temperature tendency, we diagnose the $\partial T'/\partial t$ value in the domain of 45°–55°N, 100°–125°E (i.e., a box marked in Fig. 7a). Figure 7b illustrates the contributions of each budget term to the temperature tendency averaged over this maximum $\partial T'/\partial t$ region. The leftmost bar represents the observed $\partial T'/\partial t$, whereas the remaining bars denote the five terms at the right hand side of Eq. (1). The budget analysis indicates that the observed positive temperature tendency is primarily attributed to anomalous meridional temperature advection $(-v\partial T/\partial y)'$.

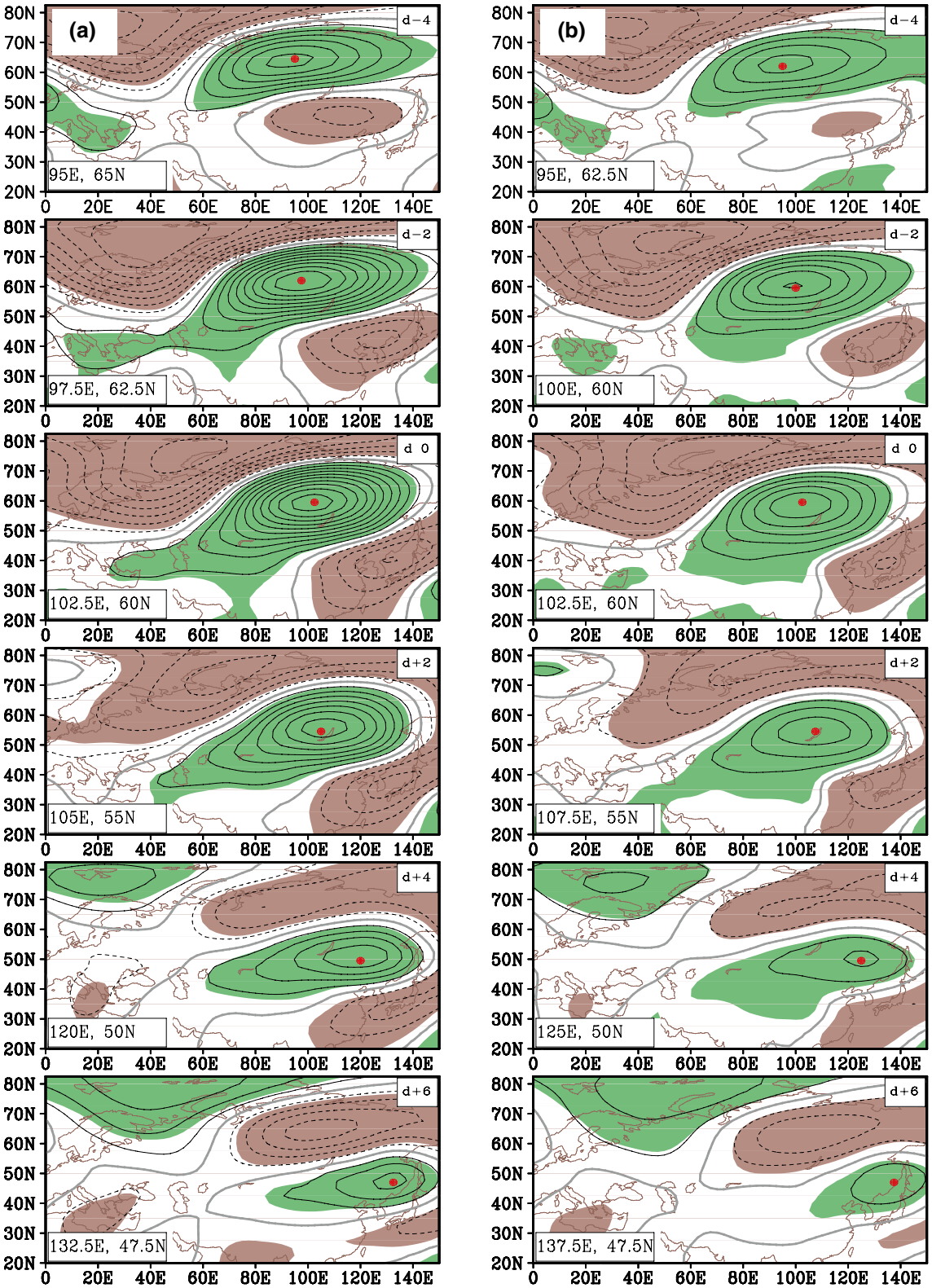

Fig. 6 **a** As in Fig. 3, but for 10–60-day 300 hPa geopotential height anomalies from day −4 to day +6, with an interval of 30 gpm. **b** As in (**a**), but for 600 hPa

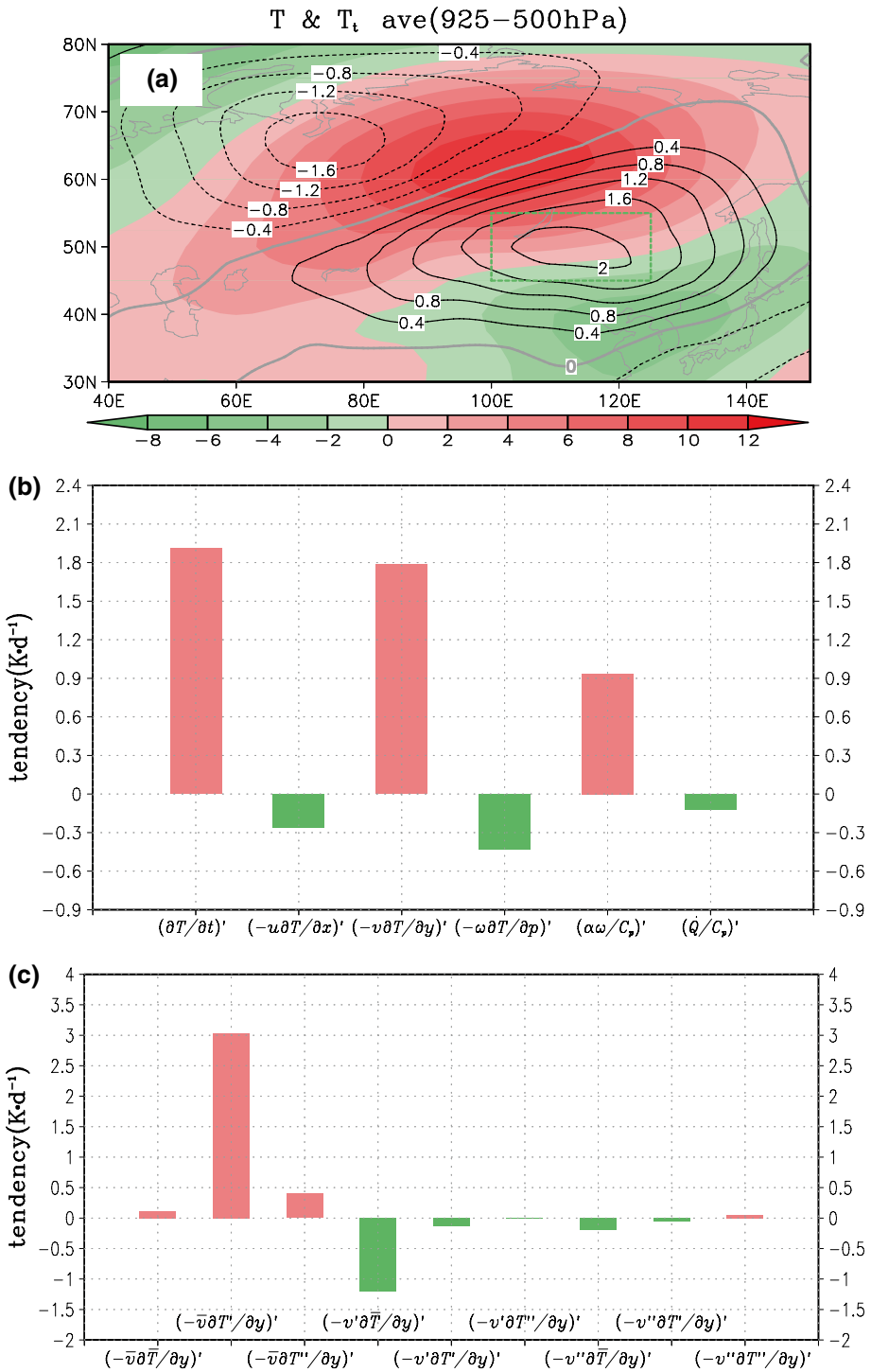

Fig. 7 **a** Horizontal distribution of T' (*shading*; unit: K) and $\partial T'/\partial t$ (*contour*; unit: K d^{-1}) for day 0 composite. The *box area* 45°–55°N, 100°–125°E indicate the center of $\partial T'/\partial t$. **b** Individual terms of $\partial T'/\partial t$ averaged in the *box* marked in (**a**) for day 0 composite. **c** Individual terms of $(-v\partial T/\partial y)'$ averaged in the *same box* for day 0 composite. All values above are of the vertical integration (925–500 hPa)

Next we examine which of nine terms at the right hand side of Eq. (2) contribute to $(-v\partial T/\partial y)'$. The diagnosis result is shown in Fig. 7c. It is clearly seen that the maximum contribution comes from $(-\bar{v}\partial T'/\partial y)'$ (bar 2 in Fig. 7c). This indicates that the primary contribution to the southeastward propagation of the temperature perturbation arises from the advection of anomalous temperature by the mean flow. This thermal advection mechanism is also clearly seen in the temperature budget analysis at day −5 to day +5.

As the temperature anomaly in the upper troposphere is opposite to that of the lower troposphere, does the same physical process control the phase propagation of upper-tropospheric T'? Figure 8b, c show 200–150 hPa integrated temperature budget terms averaged over the same box region (shown in Fig. 7a). As expected, the 200–150 hPa

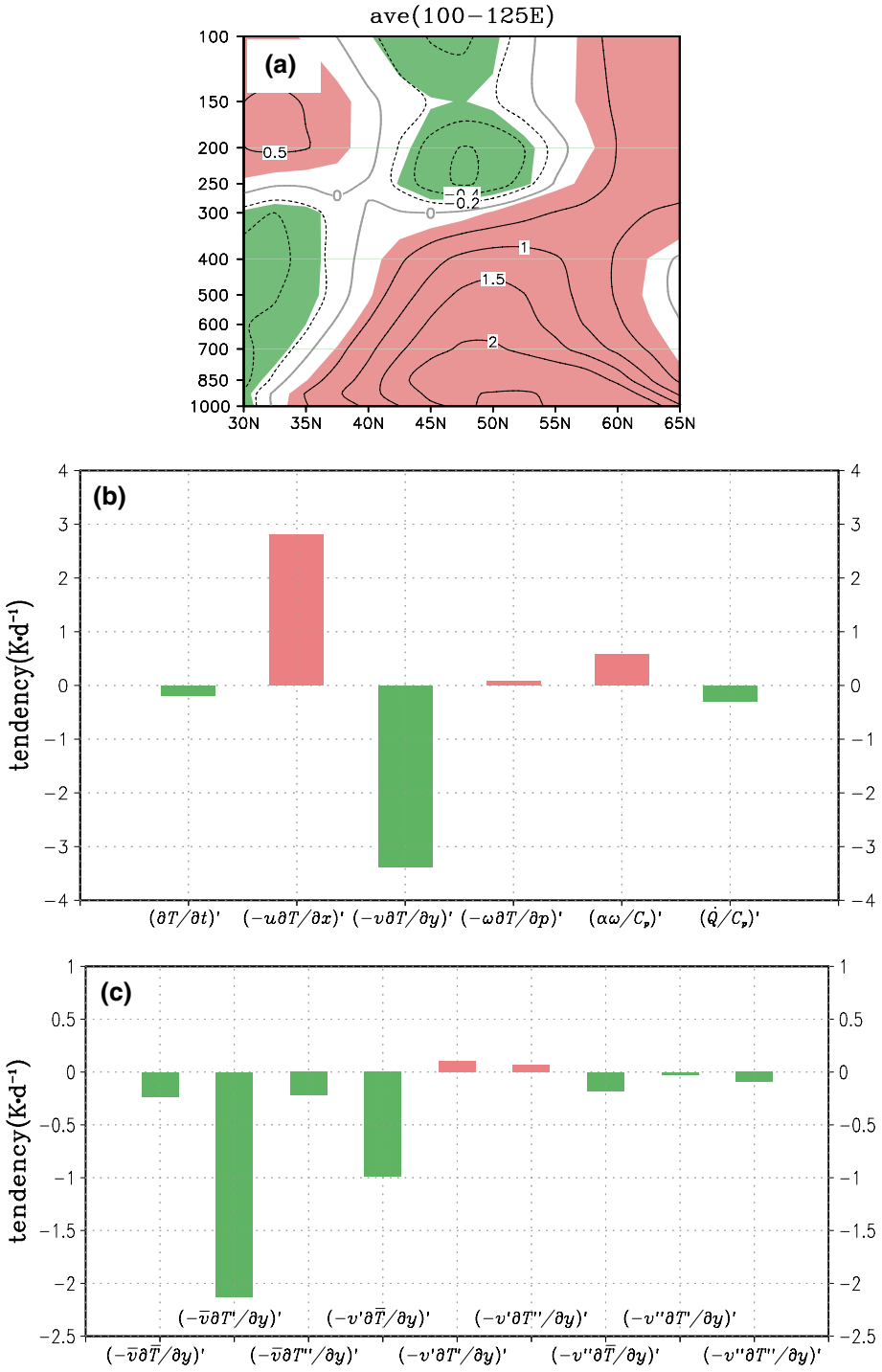

Fig. 8 **a** The latitudinal-vertical profile of the composite 10–60-day $\partial T'/\partial t$ (K d^{-1}) averaged over 100°–125°E at day 0. The *shadings* indicate significance level of 0.05. **b** Individual terms of $\partial T'/\partial t$ averaged in the *box* marked in Fig. 7a for day 0 composite. **c** Individual terms of $(-v\partial T/\partial y)'$ averaged in the *same box* for day 0 composite. All terms above are of the vertical integration (200–150 hPa)

averaged $\partial T'/\partial t$ (bar 1 in Fig. 8b) is negative. Though the negative value is small, it is of statistical significance (see shaded areas in Fig. 8a). Our upper-level temperature budget analysis shows that the main contribution still arises from $(-v\partial T/\partial y)'$ (bar 3 in Fig. 8b). The dominant term that contributes to the negative tendency $(-v\partial T/\partial y)'$ is still the advection of the temperature perturbation by the mean meridional flow, $(-\bar{v}\partial T'/\partial y)'$ (bar 2 in Fig. 8c).

Figure 9a illustrates the horizontal distributions of 925–500 hPa integrated $\bar{v}$ (vector), T' (shading) and $(-\bar{v}\partial T'/\partial y)'$ (contour) at day 0. The mean meridional wind is in general southward ($\bar{v} < 0$). At day 0, the vertically integrated lower-tropospheric temperature is positive north of 50°N. The mean northerly advects the positive temperature anomaly southward, leading to southward propagation. It is worth mentioning that maximum meridional

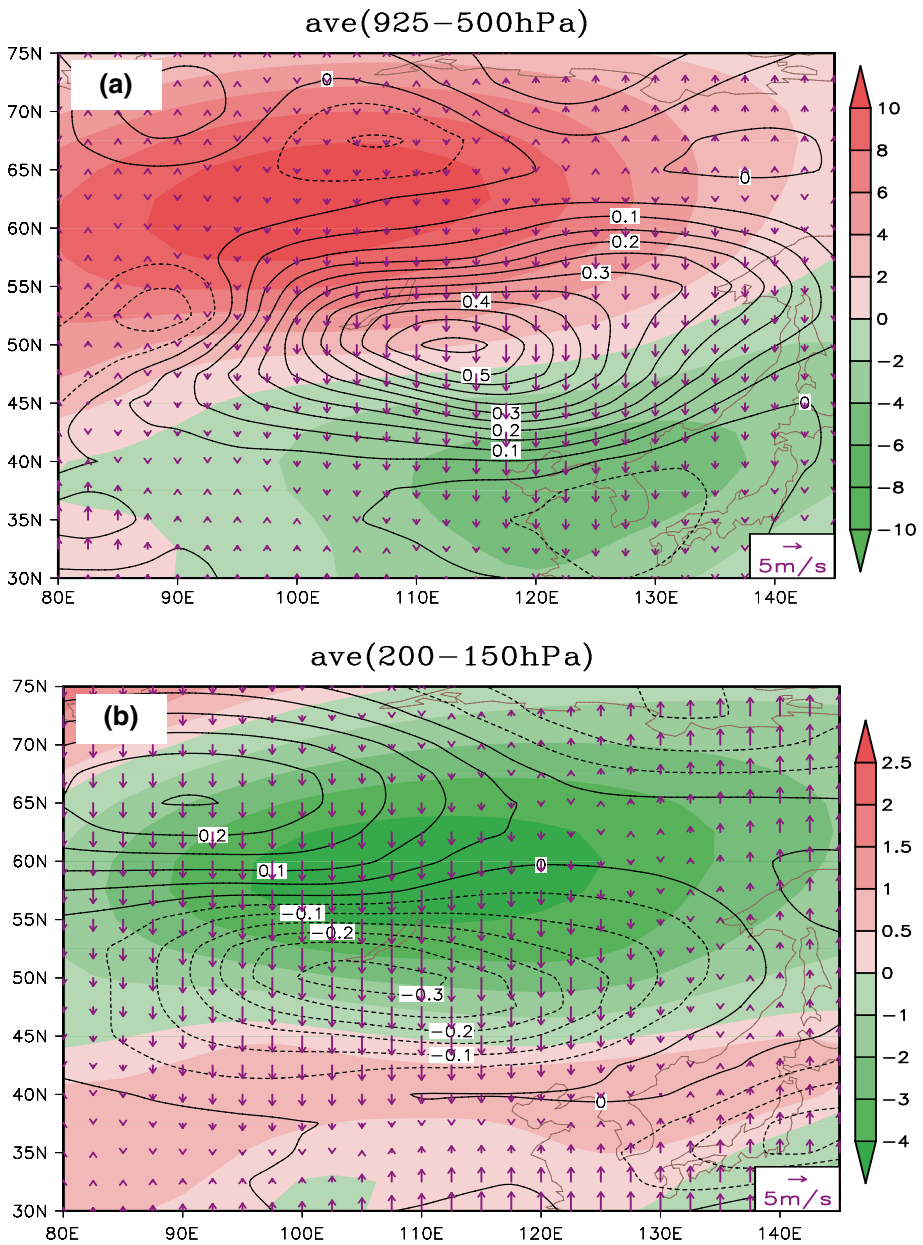

Fig. 9 **a** Horizontal distribution of 925–500 hPa averaged T' (*shading*; unit: K), the mean meridional wind $\bar{v}$ (vector; unit: m s^{-1}; see scale at the *lower right corner*), and $(-v\partial T/\partial y)'$ (contours; with an interval of 0.05 K d^{-1}) for day 0 composite. **b** As in (**a**), but for 200–150 hPa averaged values

temperature advection $(-\bar{v}\partial T'/\partial y)$ appears to the east of the positive T' center due to the product of the $\partial T'/\partial y$ and $\bar{v}$. Though the meridional temperature gradient $\partial T'/\partial y$ is approximately symmetric between west and east, the mean meridional wind $\bar{v}$ attains a greater value to the east of the positive T' center. As a result, maximum meridional temperature advection $(-\bar{v}\partial T'/\partial y)'$ appears to the southeast of the positive T' center, resulting in southeastward propagation of T'.

Figure 9b illustrates 200–150 hPa integrated $\bar{v}$, T', and $(-\bar{v}\partial T'/\partial y)'$ at day 0. The mean meridional wind also points toward the south in the region between a negative temperature anomaly to the northwest and a positive temperature anomaly to the southeast. This leads to a negative temperature tendency in between, as the mean wind advects the upper-tropospheric negative temperature anomaly southeastward. Thus, the equivalent barotropic mean flows play an important role in advecting the upper and lower tropospheric temperature perturbations southeastward.

5 Rossby wave activity flux in the upper troposphere

In Sect. 4, we focus on the temperature budget analysis and demonstrate that the southeastward propagation is caused by the anomalous advection by the mean flow. Here we shift our focus to the upper-tropospheric wave train in the

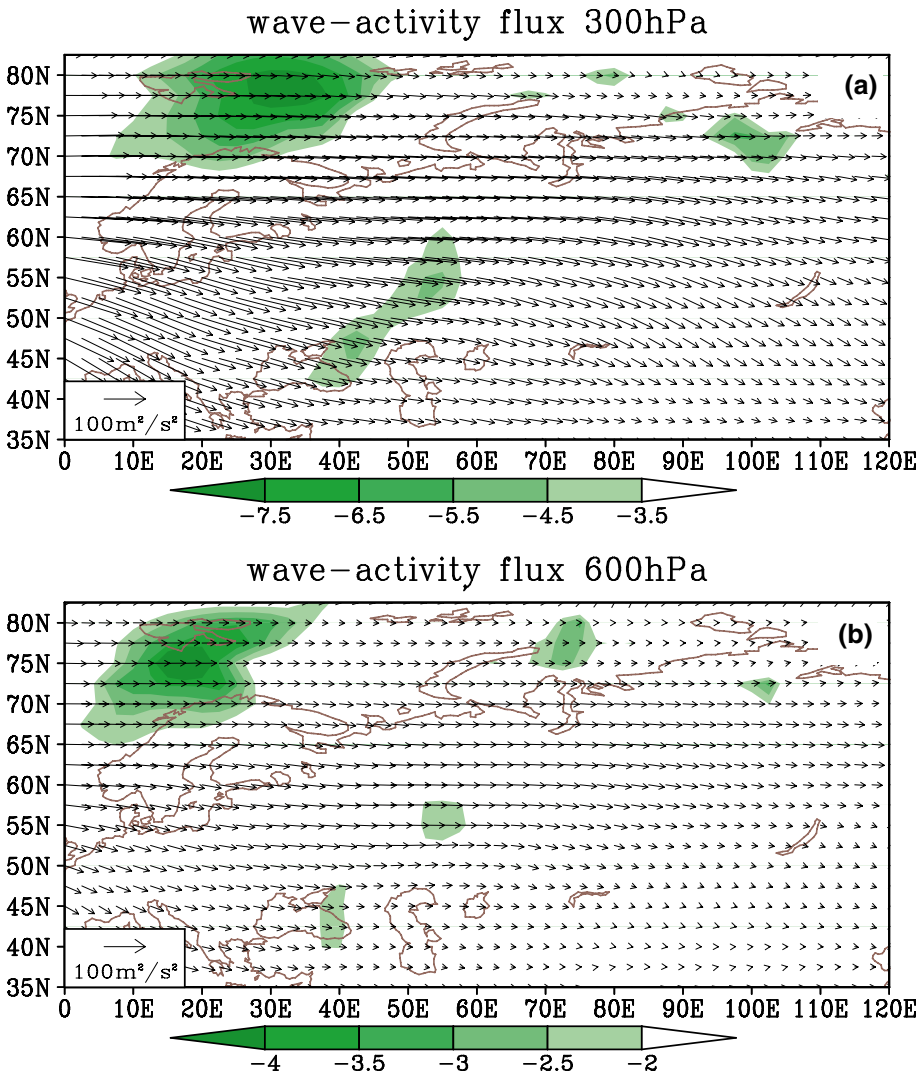

Fig. 10 **a** Horizontal evolution of wave-activity flux (vector; unit: $m^2\ s^{-2}$; see scale at the *lower left corner*) and wave flux divergence (*shading*; unit: 10^{-5} $m\ s^{-2}$; see *color bar*) at 300 hPa averaged from day –10 to day –5 during strong positive events. **b** As in (**a**), but for 600 hPa

height anomaly field (Fig. 6a). We hypothesize that the southeastward propagation of the upper-tropospheric height anomaly is a result of Rossby wave energy propagation.

To reveal this possibility, we calculated Rossby wave activity flux (WAF) and its divergence field at each level. It is found that similar WAF and its divergence appear in the upper and lower troposphere. Figure 10 shows the horizontal distributions of the WAF and its divergence fields at 300 and 600 hPa respectively. The WAF formula used here is a phase-independent wave activity flux developed by Takaya and Nakamura (2001). The shading in Fig. 10 indicates the region of large WAF convergence, implying the energy source of the wave train.

It is shown in Fig. 10 that the WAF points southeastward over most of the mid-high latitude Eurasia. An obvious wave flux convergence appears over high-latitude Europe/North Atlantic sector, suggesting that there is Rossby wave energy accumulation in the region. Thus, the wave train like pattern in the upper-tropospheric height anomaly field as shown in Fig. 6a is likely a result of Rossby wave energy dispersion, originated from the upstream high-latitude Europe/North Atlantic sector.

During the southeastward journey, the ISO perturbation may gain energy from the mean flow. To demonstrate this possibility, we calculated both kinetic and potential energy conversions between the mean flow and the ISO perturbation. Figure 11a shows the meridional-vertical distribution of $\overline{\overline{CK}}_{iso}$ (i.e., barotropic energy conversion between the ISO and the mean flow) averaged over 80°–120°E (where maximum amplitude of the intraseasonal temperature anomaly is located). Here $\overline{\overline{CK}}_{iso}$ is calculated by the sum of the four terms at the right-hand side of Eq. (3). It is obvious that the value of $\overline{\overline{CK}}_{iso}$ is positive 50°N poleward throughout the troposphere, with a maximum center at 300 hPa. This indicates that maximum energy conversion from the mean flow to the ISO perturbation occurs in the upper troposphere around 300 hPa. All the four terms at the

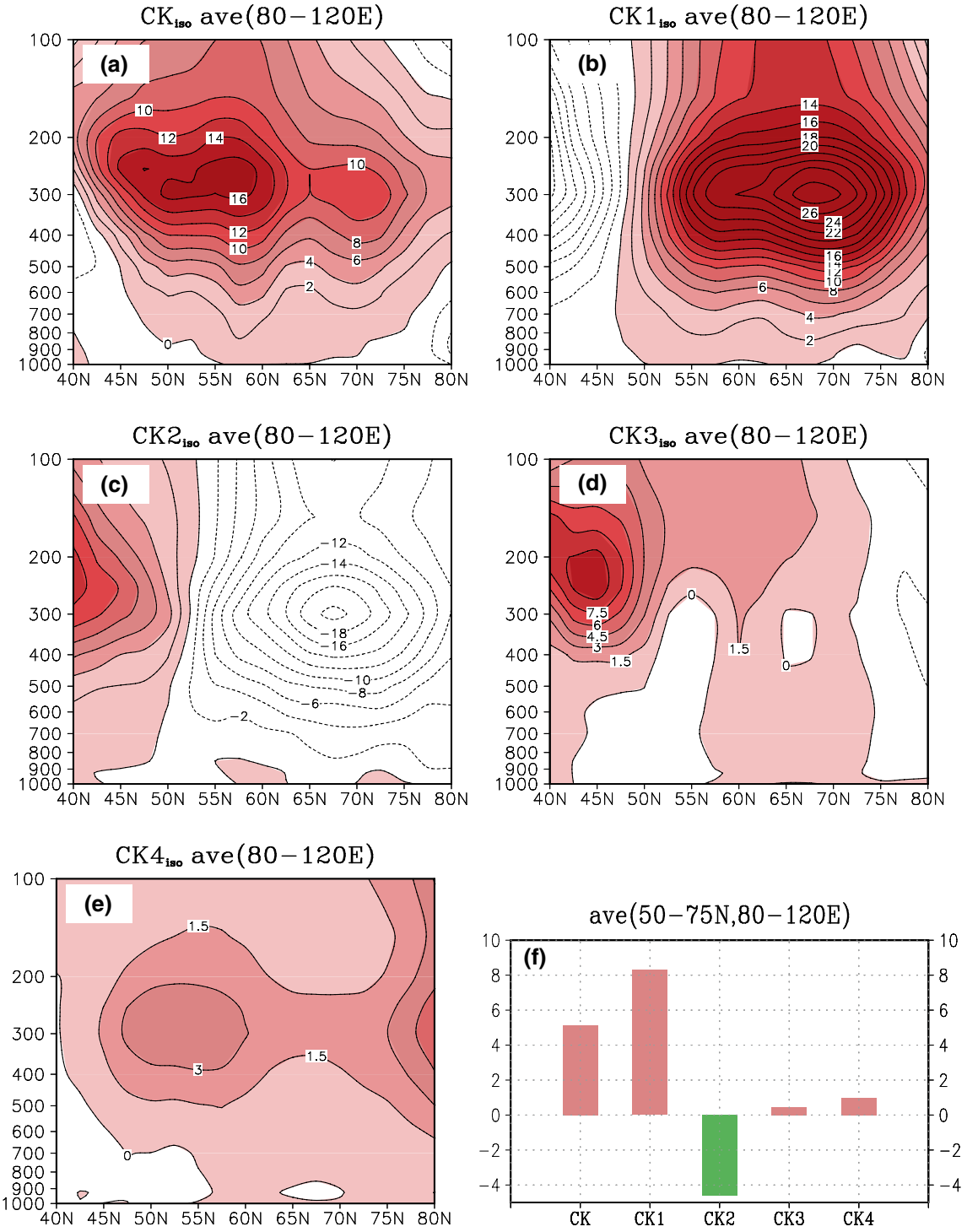

Fig. 11 **a** Meridional-vertical profile of energy conversion ($\overline{\overline{CK}}_{iso}$) between the mean flow and the ISO flow averaged over 80°–120°E in boreal winter. **b–e** As in (**a**), but for the individual terms $\overline{\overline{CK1}}_{iso}$ ($-\overline{\overline{u'^2}}\frac{\partial\bar{\bar{u}}}{\partial x}$), $\overline{\overline{CK2}}_{iso}$ ($-\overline{\overline{v'^2}}\frac{\partial\bar{\bar{v}}}{\partial y}$), $\overline{\overline{CK3}}_{iso}$ ($-\overline{\overline{u'v'}}\frac{\partial\bar{\bar{u}}}{\partial y}$) and $\overline{\overline{CK4}}_{iso}$ ($-\overline{\overline{u'v'}}\frac{\partial\bar{\bar{v}}}{\partial x}$), respectively. Positive values are *shaded*. **f** $\overline{\overline{CK}}_{iso}$ averaged from surface to 100 hPa and its individual terms averaged over the area of 50°–75°N, 80°–120°E, where the maximum amplitude of the intraseasonal temperature anomaly is located. The unit is 10^{-5} m^2 s^{-3}

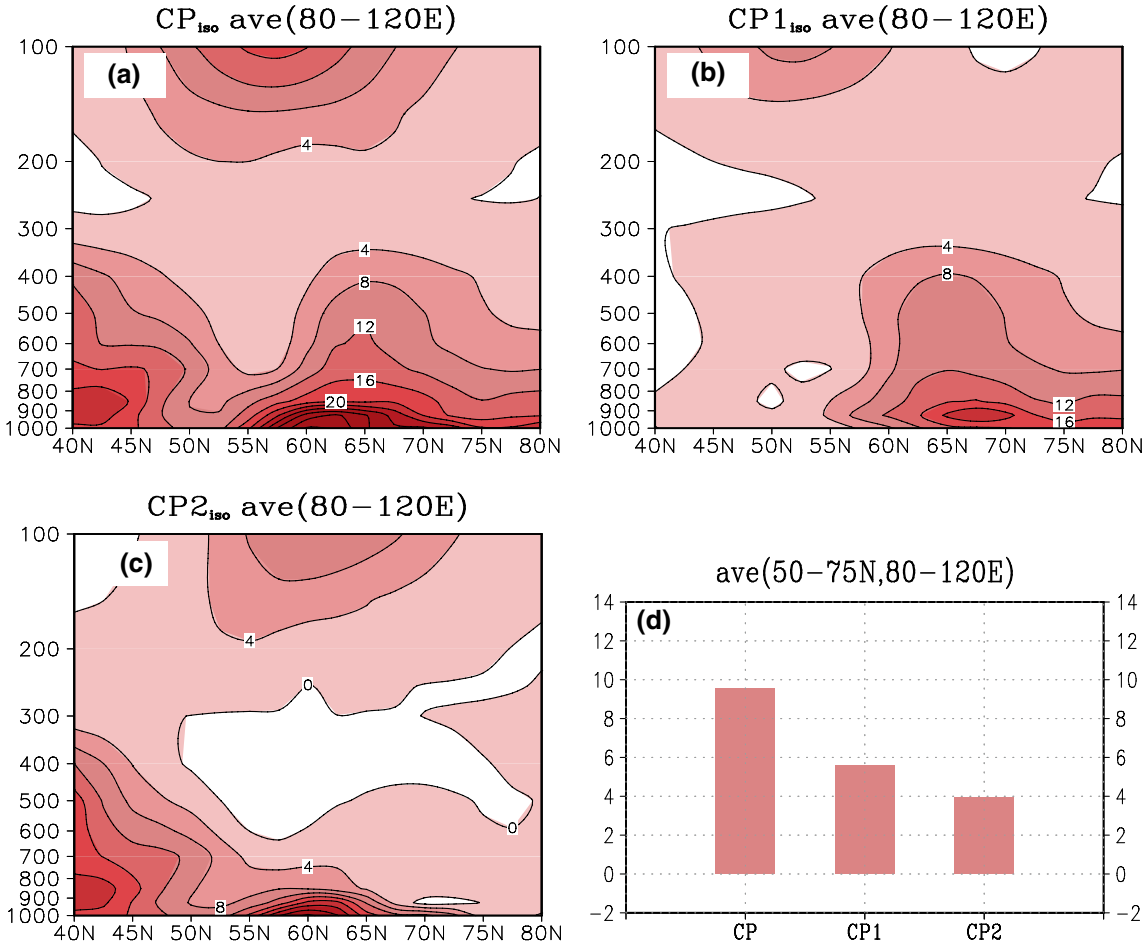

Fig. 12 **a** Meridional-vertical profile of potential energy conversion ($\overline{\overline{CP}}_{iso}$; unit: 10^{-5} m^2 s^{-3}) between the mean flow and the ISO flow averaged over 80°–120°E in boreal winter. **b**, **c** As in (**a**), but for the individual terms $\overline{\overline{CP1}}_{iso}$ $[-\frac{g}{(\gamma_d-\gamma)T_0}(\overline{\overline{u'T'}}\frac{\partial\overline{\overline{T}}}{\partial x})]$ and $\overline{\overline{CP2}}_{iso}$ $\left[-\frac{g}{(\gamma_d-\gamma)T_0}\left(\overline{\overline{v'T'}}\frac{\partial\overline{\overline{T}}}{\partial y}\right)\right]$, respectively. The above contour interval is 4 × 10^{-5} m^2 s^{-3}; positive values are *shaded*. **d** $\overline{\overline{CP}}_{iso}$ averaged from surface to 100 hPa and its individual terms (unit: 10^{-5} m^2 s^{-3}) averaged over the area of 50°–75°N, 80°–120°E

right-hand side of Eq. (3) are calculated in the same region (Fig. 11b–e). It is found that except for $\overline{\overline{CK2}}_{iso}$, all other terms contribute positively to the energy conversion.

To quantitatively assess the relative roles of the four terms, we calculated latitudinal averaged $\overline{\overline{CK}}_{iso}$ between 50°N and 75°N (i.e., the region of maximum ISO activity shown in Fig. 1c). The latitudinal-averaged value of each term averaged from surface to 100 hPa (Fig. 11f) shows that the major contribution is the first term $\overline{\overline{CK1}}_{iso}$ $(-\overline{\overline{u'^2}}\frac{\partial\overline{\overline{u}}}{\partial x})$. Because $-\overline{\overline{u'^2}}$ is always negative, the sign of $-\overline{\overline{u'^2}}\frac{\partial\overline{\overline{u}}}{\partial x}$ is determined by $\frac{\partial\overline{\overline{u}}}{\partial x}$. The mean zonal wind is mainly convergent (i.e., negative $\frac{\partial\overline{\overline{u}}}{\partial x}$) over the region of interest (figure omitted). This is why $\overline{\overline{CK1}}_{iso}$ $(-\overline{\overline{u'^2}}\frac{\partial\overline{\overline{u}}}{\partial x})$ is mostly positive in the region of interest. The second leading contribution is the fourth term $\overline{\overline{CK4}}_{iso}$ $(-\overline{\overline{u'v'}}\frac{\partial\overline{\overline{v}}}{\partial x})$. Further examination shows that the sign of $-\overline{\overline{u'v'}}$ and $\partial\overline{\overline{v}}/\partial x$ generally is the same over the vast region of mid- and high-latitude Asia, especially the area of maximum amplitude of the intraseasonal temperature perturbation (not shown). Physically, the in-phase relationship implies that the pressure troughs/ridges associated with the ISO perturbation tilts southwestward in the region of anticyclonic shear of mean meridional wind, and vice versa. The above analyses indicate that both the zonal shear of mean meridional wind and the zonal convergence of mean zonal wind play important roles in promoting barotropic kinetic energy conversion from the mean flow to the ISO flow.

According to Eq. (4), we further calculated the $\overline{\overline{CP}}_{iso}$ (i.e., potential energy conversion between the mean flow and the ISO flow), and the results are shown in Fig. 12. It can be seen from Fig. 12a that there is positive potential energy transfer from the mean flow to the ISO flow in the

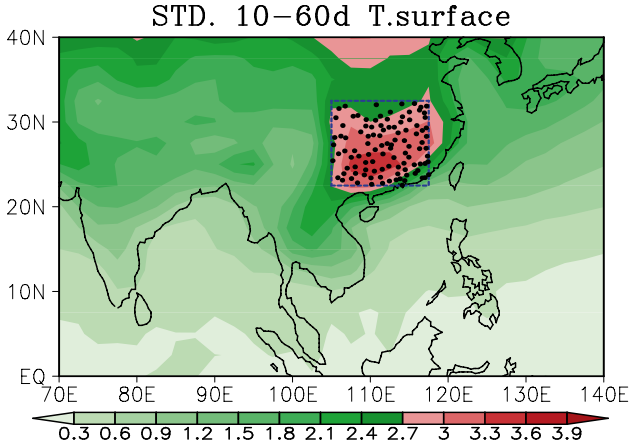

Fig. 13 Standard deviation of 10–60-day surface temperature anomalies (*shading*; unit: K) in boreal winter. The reason why this maximum variability center is not apparent in Fig. 1e is due to *different color scales* used. The *solid dots* in the *box area* of 22.5°–32.5°N, 105°–117.5°E indicate the position of the 106 ground observational stations of China. The area-averaged temperature anomaly of the 106 stations is a target of extended-range forecast

region of interest. Consistent with maximum temperature anomaly near the surface, maximum energy conversion is also confined in the lower troposphere. The contribution from each term at the right-hand side of Eq. (4) is displayed in Fig. 12b–c. It shows that both the individual terms contribute positively to the potential energy conversion. A further diagnosis discloses that both eddy heat flux transport and the mean thermal gradient play important roles in promoting such potential energy conversion (Fig. 12d).

The energy conversion diagnoses above indicate that the intraseasonal wave perturbation gains energy from the mean flow through both kinetic and potential energy conversions. Because of such energy conversion, the upper-tropospheric and lower-tropospheric ISO perturbations may maintain their strength against natural dissipation during their southeastward journey.

6 Extended-range (10–30-day) temperature prediction with a multivariate regression model

The composite evolution maps in Fig. 3 suggest that low-frequency temperature fluctuation in East Asia is greatly influenced by the southeastward propagating ISO signal. This motivates us to construct a physics-based empirical model for extended-range (10–30-day) winter temperature prediction. Figure 13 illustrates the STD of 10–60-day temperature anomalies in winter. Note that a maximum temperature variability center appears over southeast China (22.5°–32.5°N, 105°–117.5°E). Figure 13 shows clearly that the standard deviation of 10–60-day surface temperature anomalies in the box region is much greater than the vicinity regions. This is also the most populated region in China. Thus, the area-averaged temperature anomaly in this region becomes a target of the extended-range forecast. A similar forecast model can be constructed for other regions of China.

Table 1 List of predictors for the multivariate regression model at different lead times

Lead time	Predictors
5 days	u850 (40°–55°N, 60°–105°E) − u850 (65°–75°N, 60°–115°E) Z500 (40°–50°N, 80°–110°E) − Z500 (57.5°–70°N, 65°–105°E) u200 (47.5°–60°N, 80°–110°E) − u200 (70°–80°N, 70°–105°E)
10 days	u850 (52.5°–60°N, 70°–90°E) − u850 (70°–77.5°N, 50°–70°E) Z500 (40°–50°N, 75°–95°E) − Z500 (55°–70°N, 40°–60°E) u200 (55°–67.5°N, 70°–105°E) − u200 (70°–85°N, 40°–70°E)
15 days	u850 (57.5°–65°N, 65°–95°E) − u850 (70°–82.5°N, 30°–45°E) Z500 (40°–57.5°N, 67.5°–100°E) − Z500 (55°–72.5°N, 20°–40°E) u200 (60°–70°N, 60°–105°E) − u200 (40°–52.5°N, 75°–120°E)
20 days	u850 (60°–70°N, 65°–110°E) − u850 (80°–87.5°N, 65°–95°E) Z500 (47.5°–60°N, 70°–100°E) − Z500 (50°–67.5°N, 10°–20°E) u200 (62.5°–75°N, 65°–95°E) – u200 (45°–52.5°N, 85°–120°E)
25 days	u850 (62.5°–72.5°N, 60°–110°E) Z500 (57.5°–70°N, 82.5°–100°E) u200 (70°–77.5°N, 80°–100°E) − u200 (50°–60°N, 90°–105°E)
30 days	u850 (70°–80°N, 80°–110°E) − u850 (50°–57.5°N, 80°–105°E) Z500 (62.5°–72.5°N, 75°–105°E) u200 (72.5°–85°N, 70°–110°E) − u200 (50°–62.5°N, 70°–120°E)

The zonal wind and geopotential height anomalies averaged over the specified region shown in this table are used as predictors. To reduce the predictor numbers, the signals in different regions are combined into one predictor by taking their differences

For practical application, we first applied the non-filtering method to the surface temperature data. An EOF analysis to the non-filtered field (denoted as T'^{*}) was then conducted in a way similar to that in Sect. 3. The lead-lagged regression of T'^{*} against $PC1^{*}$ from day −8 to day +10 shows a similar southeastward propagation feature, suggesting that the non-filtering method works well and can be used to extract the intraseasonal (10–60-day) signals.

Next a multivariate regression (MVR) model is constructed to predict area-averaged intraseasonal temperature anomaly over southeast China at a lead time of 5–30 days

(with a 5-day interval). The surface temperature anomalies averaged over 106 ground stations over 22.5°–32.5°N, 115°–117.5°E are used as predictand. The locations of the 106 stations were plotted in Fig. 13 (see solid dots). For each forecast lead, we select statistically significant signals at 850, 500 and 200 hPa levels as predictors. In the MVR model, the zonal wind and geopotential height anomalies averaged over a specified region (shown in Table 1) are used as predictors. The winter months DJFM for the period from 1979/80 to 2003/04 ($25 \times 121 = 3025$ days) are used as a training period to construct the model. Then a 10-yr (from 2004/05 to 2013/14, total $10 \times 121 = 1210$ days) independent forecast is further performed, to assess the model forecast skill.

The MVR model is constructed for each lead time, and the potential predictors are selected based on lagged correlation between the predictand and large-scale predictors over 20°–90°N, 10°–140°E in DJFM from 1979/80 to 2003/04 (Fig. 14). The predictors capture well the southeast propagating signals. To gain stable and reliable forecast results, we select the predictors whose lagged correlation coefficients are not only of large value but also extending to a large area in space. If a variable contains significant signals in different regions at a given lead time, we take their difference (if with an opposite sign) to reduce the predictor numbers. The predictors for each lead time are given in Table 1.

The extended-range predictions are made for every 5 days (i.e., December 1st, December 6th, December 11th, … February 19th, February 24th, March 1st). The predictand is predicted for all lead times (say, day 5, 10, 15, … 30) at once. For example, for March 1st forecast, we predict the temperature anomaly on March 6th, March 11th, March 16th, March 21th, March 26th, and March 31th, respectively. Thus, for each lead time, there are 190 time points (19 points × 10 winters) from 2004/05 to 2013/14.

Figure 15a shows 10-yr independent forecast results. It displays the temporal correlation coefficients (TCC, blue line) between the observed and the predicted 10–60-day temperature anomalies and the standardized root-mean-square error (RMSE, red line) as the function of lead time. Here the RMSE has been normalized by a standard deviation of the observed temperature anomalies, so that a unit RMSE corresponds to an error of one standard deviation of the observed temperature anomalies. Figure 15a shows that the TCC value is above 0.36 for the lead time of up to 25 days. Here 0.36 represents 0.05 significance level. It is interesting to note that the TCC reaches a higher value (~0.40) at lead times of 25 days than that of 15–20 days. The exact reason to cause that is unknown, and deserves a further study. The standardized RMSE at all lead times is around 1.0–1.2, as shown by the right axis in Fig. 15a, indicating the stable forecast errors of amplitude by the MVR model.

The normalized time series of the 25-day lead forecast of area-averaged temperature anomaly over southeast China and the corresponding observation are exhibited in Fig. 15b. The temporal correlation coefficient between the observed and forecasted time series is ~0.4. Even at such a long lead, the forecasted amplitudes are quite close to the observed. The 10-yr independent forecast result above indicates a high skill for extended-range forecast of the intraseasonal temperature anomalies over southeast China. The major predictability source lies in upstream ISO signals that propagate southeastward across the mid-high latitude Eurasia Continent.

7 Summary and discussion

In this study, we examined the 3-dimensional structure and evolution characteristics of intraseasonal (10–60-day) temperature disturbances over mid-high latitude Eurasia during boreal winter, by using daily NCEP-NCAR reanalysis data. It was found that the maximum variability center of intraseasonal temperature anomalies appear at lower troposphere over the region of 50°–75°N, 80°–120°E in boreal winter. Using the combined EOF and composite analysis method and the local lead-lag correlation map, we reveal that the temperature perturbation propagates southeastward at a averaged meridional phase speed of 2.5 m s^{-1} and zonal phase speed of 3.2 m s^{-1}.

In contrast to maximum intraseasonal temperature anomaly near the surface, maximum geopotential height anomaly, as well as maximum stream function anomaly, appears in the upper troposphere (at 300 hPa). The temperature and geopotential height anomalies are well in hydrostatic relationship, and they both propagate southeastward.

The cause of the southeastward propagation of the temperature anomaly is examined through a thermodynamic budget diagnosis. It is found that a negative (positive) temperature tendency appears to the southeast of a negative (positive) intraseasonal temperature anomaly center throughout the troposphere. The temperature budget analysis indicates that the dominant term that contributes to the observed southeastward shift of the temperature tendency over the activity center is the advection of the temperature anomaly by the meridional mean flow. Those point out the important role of the ISO-mean flow interaction in causing the southeastward propagation.

A wave activity flux analysis indicates that the southeastward propagating wave train is likely a result of Rossby wave energy propagation, as the wave-activity flux points toward the ISO propagation direction. The energy source of the Rossby waves appears at the high latitude Europe/

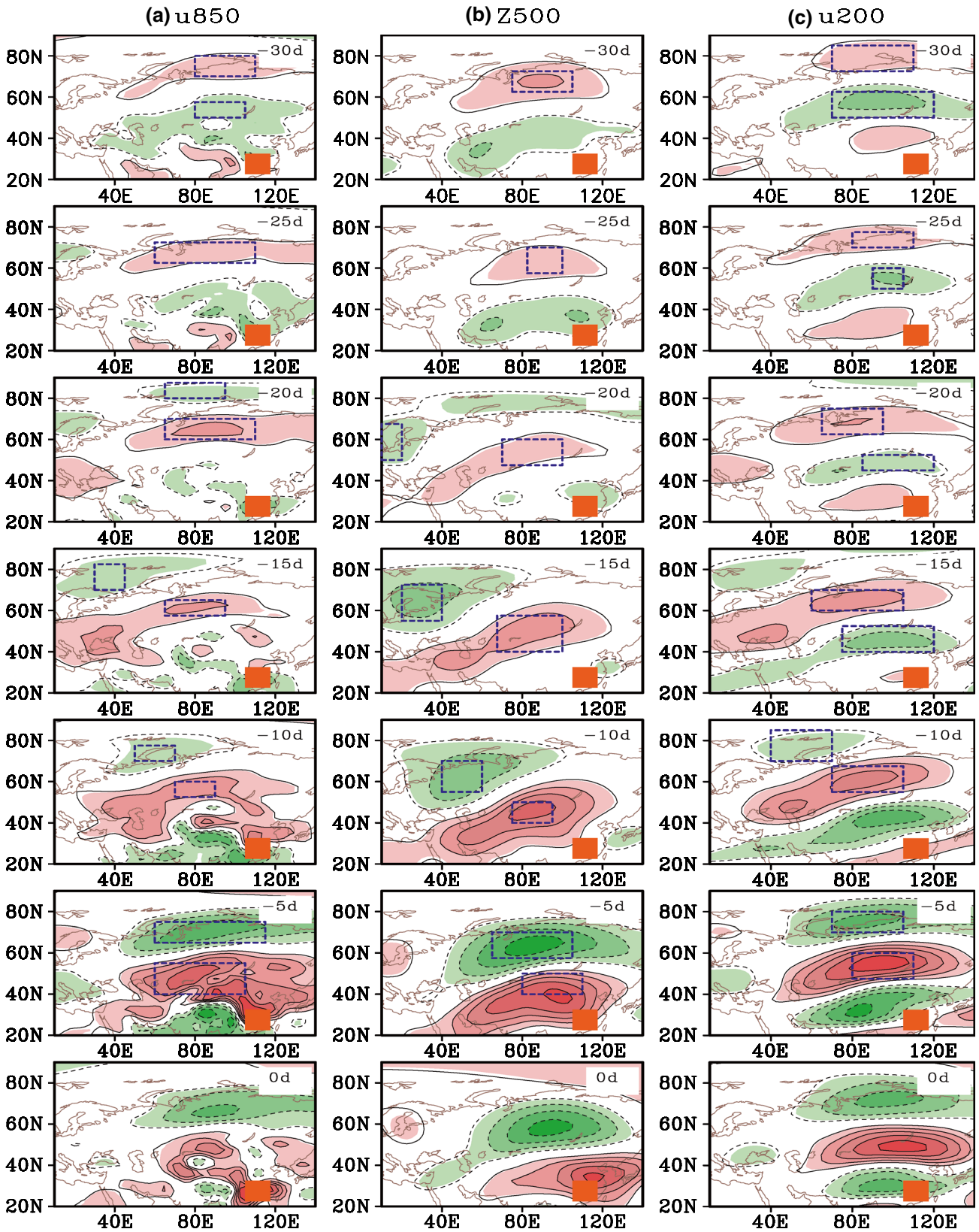
(a) u850
(b) Z500
(c) u200
−30d
−25d
−20d
−15d
−10d
−5d
0d
80N
60N
40N
20N
40E
80E
120E

◀ **Fig. 14** Lag correlation coefficients (contour; interval: 0.15) between the 10–60-day station temperature anomaly averaged in the *orange box area* of 22.5°–32.5°N, 115°–117.5°E and large-scale predictors of **a** *u*850, **b** *Z*500, **c** *u*200 from −30 to 0 days (from top to bottom; with an interval of 5-day) in DJFM from 1979/80 to 2003/04. *Pink* (*green*) *shading* indicates positive (negative) correlation coefficient exceeding 0.05 significance level. The *dashed boxes* denote the area of predictors shown in Table 1

Atlantic sector, where maximum wave activity flux convergence resides.

The observational analyses suggest that both the mean flow induced anomalous temperature advection and upper-tropospheric Rossby wave energy dispersion play a role in the southeastward propagation. A further analysis of energy conversion demonstrates that the ISO perturbation gains energy from the mean flow during its southeastward journey, through both barotropic kinetic energy conversion and potential energy conversion. Maximum barotropic kinetic energy conversion appears in the upper troposphere around 300 hPa. This feature differs markedly from the summertime tropical western North Pacific, where maximum barotropic energy conversion appears in the lower troposphere (e.g., Hsu and Li 2011). A further decomposition of barotropic energy conversion terms shows that the major contribution comes from the zonal shear of mean meridional wind and the zonal convergence of mean zonal wind. The potential energy conversion, on the other hand, has a maximum in the lower troposphere (near the surface). Both eddy heat flux and mean thermal gradient play important roles in promoting the potential energy conversion.

A multi-variate lag-regression model was constructed to assess the predictability of intraseasonal temperature anomalies in winter over East Asia. The major predictability source is the southeastward-propagating ISO signal. A 10-yr (2004–2013) independent forecast shows that the average low-frequency temperature anomaly over southeast China is highly predictable (with a temporal correlation coefficient exceeding 0.05 significance level), up to a lead of 25 days. The root mean square errors of amplitude are generally stable across all lead times (from 5 to 30 days). Therefore, it is useful to apply this methodology to real-time extended-range winter temperature forecast over China. It is worth mentioning that a non-filtering method was used in the above hindcast experiment. While such a method is not as accurate as the traditional band-pass filter method for extracting the ISO signal, the correlation coefficient between the two temperature series with the two methods is about 0.8. The result is consistent with Hsu et al. (2015).

In the current empirical model, the predictors are selected only from the mid-high latitude ISO signals. What

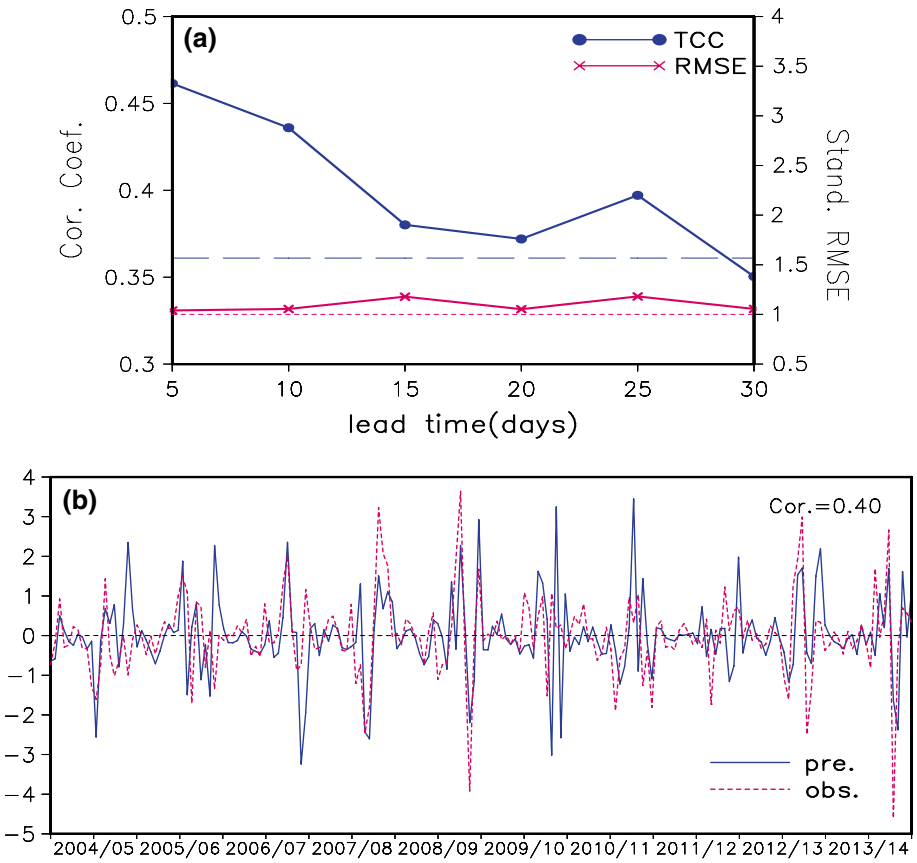

Fig. 15 **a** The temporal correlation coefficients (i.e., TCC; *blue line*; left axis) between observed and predicted 10–60-day temperature anomaly and the standard RMSE (*red line*; right axis) of the predicted temperature as the function of forecast leading time days. *Blue dashed line* means the 0.05 significance level of the correlation coefficient; *red dashed line* denotes one standard RMSE. **b** The normalized prediction (*solid line*) and observation (*dashed line*) of the 10–60-day temperature anomaly at 25-day forecast in advance in DJFM from 2004/05 to 2013/14. The number at the *upper-right corner* denotes the correlation coefficient between them

happens to the forecast skill if one only selects the low latitude low-frequency signals as predictors? To address this question, we select a real-time multivariate MJO index (RMM1, RMM2) constructed by Wheeler and Hendon (2004) as predictors to forecast the surface temperature anomalies over the same southeast China region. The TCC values for the lead time of 5-, 10-, 15-, 20-, 25-, and 30-day are about 0.20, 0.12, −0.02, 0.02, 0.14, and 0.08, respectively. Although the TCC at 25-day lead is greater than that of 15- and 20-day lead, all of them are not of statistical significance. Therefore, the real-time multivariate MJO index shows lower skill compared to the mid-latitude predictors. This implies that to the first order, the winter intraseasonal temperature variability over southeast China is determined by signals from north rather than from the south. However, the connection between the mid-high latitude ISO signals and the MJO needs to be further investigated.

It is worth mentioning that the current barotropic kinetic and potential energy conversion calculation excludes the effect of high-frequency (such as synoptic-scale) eddies. It should be interesting to investigate the energy conversions in a multi-scale interactive framework as discussed in Hsu and Li (2011) and Zhou et al. (2012). Such an effort will be done in future work. It is also worth mentioning that the zonal phase propagation of the winter ISO perturbation over the Eurasia is very different from that of the summer ISO perturbation over North Pacific (see Wang et al. 2013). Is the opposite zonal phase propagation caused by different mean flow or perturbation structure? A further in-depth analysis is needed to reveal the dynamics origin of the difference.

Acknowledgments The authors are grateful to anonymous reviewers for their constructive comments. This work was supported by China National 973 project 2015CB453200, NSFC grant 41475084, NRL grant N00173-13-1-G902, Jiangsu Shuang-Chuang Team, and the Priority Academic Program Development of Jiangsu Higher Education Institutions (PAPD). This is SOEST contribution number 9553, IPRC contribution number 1163, and ESMC contribution number 82.

References

Anderson JR, Rosen RD (1983) The latitude-height structure of 40–50 day variations in atmospheric angular momentum. J Atmos Sci 40:1584–1591

Annamalai H, Slingo J (2001) Active/break cycles: diagnosis of the intraseasonal variability of the Asian summer monsoon. Clim Dyn 18:85–102

Bi M, Li T, Peng M, Shen X (2015) Interactions between Typhoon Megi (2010) and a low-frequency monsoon gyre. J Atmos Sci 72:2682–2702

Bretherton CS, Smith C, Wallace JM (1992) An intercomparison of methods for finding coupled patterns in climate data. J Clim 5:541–560

Bretherton CS, Widmann M, Dymnikov VP, Wallace JM, Bladé I (1999) The effective number of spatial degrees of freedom of a time-varying field. J Clim 12:1990–2009

Cao X, Li T, Peng M, Chen W, Chen G (2014) Effects of monsoon trough interannual variation on tropical cyclogenesis over the western North Pacific. Geophys Res Lett 41:4332–4339

Chatterjee P, Goswami BN (2004) Structure, genesis and scale selection of the tropical quasi-biweekly mode. Q J R Meteorol Soc 130:1171–1194

Chen TC, Wang SY, Yen MC, Clark AJ (2009) Impact of the intraseasonal variability of the western North Pacific large-scale circulation on tropical cyclone tracks. Weather Forecast 24:646–666

Duchon C (1979) Lanczos filtering in one and two dimensions. J Appl Meteorol 18:1016–1022

Fu B, Li T, Peng M, Weng F (2007) Analysis of tropical cyclogenesis in the Western North Pacific for 2000 and 2001. Weather Forecast 33:763–780

Ghil M, Mo K (1991) Intraseasonal oscillations in the global atmosphere. Part I: Northern Hemisphere and tropics. J Atmos Sci 48:752–779

Hall JD, Matthews AJ, Karoly DJ (2001) The modulation of tropical cyclone activity in the Australian region by the Madden–Julian oscillation. Mon Weather Rev 129:2970–2982

He J, Lin H, Wu Z (2011) Another look at influences of the Madden–Julian Oscillation on the wintertime East Asian weather. J Geophys Res 116:D0319. doi:10.1029/2010JD014787

Hendon HH, Salby ML (1994) The life cycle of the Madden–Julian oscillation. J Atmos Sci 51:2225–2237

Holton JR (1992) An introduction to dynamic meteorology. Academic Press, London, p 511

Hsu PC, Li T (2011) Interactions between boreal summer intraseasonal oscillations and synoptic-scale disturbances over the western north pacific. Part I: Energetics diagnosis. J Clim 24:927–941

Hsu PC, Li T (2012) Role of the boundary layer moisture asymmetry in causing the eastward propagation of the Madden–Julian oscillation. J Clim 25:4914–4931

Hsu PC, Li T, You L, Gao J, Ren HL (2015) A spatial-temporal projection model for 10–30 day rainfall forecast in South China. Clim Dyn 44:1227–1244

Jeong JH, Kim BM, Ho CH, Noh YH (2008) Systematic variation in wintertime precipitation in East Asia by MJO-induced extratropical vertical motion. J Clim 21:788–801

Jiang X, Waliser DE (2008) Northward propagation of the subseasonal variability over the eastern Pacific warm pool. Geophys Res Lett 35:L09814

Jiang X, Li T, Wang B (2004) Structures and mechanisms of the northward propagating boreal summer intraseasonal oscillation. J Clim 17:1022–1039

Jones C, Carvalho LM, Wayne Higgins R, Waliser DE, Schemm JE (2004) A statistical forecast model of tropical intraseasonal convective anomalies. J Clim 17:2078–2095

Kajikawa Y, Yasunari T (2005) Interannual variability of the 10–25- and 30–60-day variation over the South China Sea during boreal summer. Geophys Res Lett 32:L04710. doi:10.1029/2004GL021836

Kalnay E, Kanamitsu M, Kistler R, Collins W, Deaven D, Gandin L, Iredell M, Saha S, White G, Woollen J (1996) The NCEP/NCAR 40-year reanalysis project. Bull Am Meteorol Soc 77:437–471

Kessler WS (2002) Is ENSO a cycle or a series of events? Geophys Res Lett 29:232125. doi:10.1029/2002GL015924

Kikuchi K, Wang B (2009) Global perspective of the quasi-biweekly oscillation. J Clim 22:1340–1359

Kiladis GN, Wheeler M (1995) Horizontal and vertical structure of observed tropospheric equatorial Rossby waves. J Geophys Res 100:22981–22997

Knutson TR, Weickmann KM (1987) 30–60 day atmospheric oscillations: composite life cycles of convection and circulation anomalies. Mon Weather Rev 115:1407–1436

Krishnamurti T, Gadgil S (1985) On the structure of the 30 to 50 day mode over the globe during FGGE. Tellus 37A:336–360

Lau KM, Chan PH (1986) Aspects of the 40–50 day oscillation during the northern summer as inferred from outgoing longwave radiation. Mon Weather Rev 114:1354–1367

Lau KH, Lau NC (1990) Observed structure and propagation characteristics of tropical summertime synoptic scale disturbances. Mon Weather Rev 118:1888–1913

Lengaigne M, Guilyardi E, Boulanger JP, Menkes C, Delecluse P, Inness P, Cole J, Slingo J (2004) Triggering of El Niño by westerly wind events in a coupled general circulation model. Clim Dyn 23:601–620

Li T (2014) Recent advance in understanding the dynamics of the Madden–Julian oscillation. Acta Meteorol Sinica 28:1–33

Li T, Wang B (1994) A thermodynamic equilibrium climate model for monthly mean surface winds and precipitation over the tropical Pacific. J Atmos Sci 51:1372–1385

Li T, Wang B (2005) A review on the western North Pacific monsoon: synoptic-to-interannual variabilities. Terr Atmos Ocean Sci 16:285–314

Li T, Zhou C (2009) Planetary scale selection of the Madden–Julian oscillation. J Atmos Sci 66:2429–2443

Lin A, Li T (2008) Energy spectrum characteristics of boreal summer intraseasonal oscillations: climatology and variations during the ENSO developing and decaying Phases. J Clim 21:6304–6320

Lorenz DJ, Hartmann DL (2006) The effect of the MJO on the North American monsoon. J Clim 19:333–343

Madden RA, Julian PR (1971) Detection of a 40–50-day oscillation in the zonal wind in the tropical Pacific. J Atmos Sci 28:702–708

Madden RA, Julian PR (1972) Description of global-scale circulation cells in the tropics with a 40–50 day period. J Atmos Sci 29:1109–1123

Madden RA, Julian PR (1994) Observations of the 40–50 day tropical oscillation-a review. Mon Weather Rev 122:814–837

Mak M, Cai M (1989) Local barotropic instability. J Atmos Sci 46:3289–3311

Maloney ED (2009) The moist static energy budget of a composite tropical intraseasonal oscillation in a climate model. J Clim 22:711–729

Maloney ED, Hartmann DL (2000) Modulation of eastern North Pacific hurricanes by the Madden–Julian oscillation. J Clim 13:1451–1460

Maloney ED, Hartmann DL (2001) The Madden–Julian oscillation, barotropic dynamics, and North Pacific tropical cyclone formation. Part I: observations. J Atmos Sci 58:2545–2558

Mao J, Sun Z, Wu G (2010) 20–50-day oscillation of summer Yangtze rainfall in response to intraseasonal variations in the subtropical high over the western North Pacific and South China Sea. Clim Dyn 34:747–761

Matthews AJ (2000) Propagation mechanisms for the Madden–Julian Oscillation. Q J R Meteorol Soc 126:2637–2651

Murakami M (1980) Empirical orthogonal function analysis of satellite-observed outgoing longwave radiation during summer. Mon Weather Rev 108:205–222

North GR, Bell TL, Cahalan RF, Moeng FJ (1982) Sampling errors in the estimation of empirical orthogonal functions. Mon Weather Rev 110:699–706

Shinoda T, Han W (2005) Influence of the Indian Ocean dipole on atmospheric subseasonal variability. J Clim 18:3891–3909

Simmons AJ, Wallace JM, Branstator GW (1983) Barotropic wave propagation and instability, and atmospheric teleconnection patterns. J Atmos Sci 40:1363–1392

Slingo JM, Rowell DP, Sperber KR, Nortley F (1999) On the predictability of the interannual behaviour of the Madden–Julian Oscillation and its relationship with El Niño. Q J R Meteorol Soc 125:583–609

Sperber KR (2003) Propagation and the vertical structure of the Madden–Julian oscillation. Mon Weather Rev 131:3018–3303

Takaya K, Nakamura H (2001) A formulation of a phase-independent wave-activity flux for stationary and migratory quasigeostrophic eddies on a zonally varying basic flow. J Atmos Sci 58:608–627

Tam CY, Li T (2006) The origin and dispersion characteristics of the observed tropical summertime synoptic-scale waves over the Western Pacific. Mon Weather Rev 134:1630–1646

Teng H, Wang B (2003) Interannual variations of the boreal summer intraseasonal oscillation in the Asian-Pacific region. J Clim 16:3572–3584

Wang B (1988) Dynamics of tropical low-frequency waves: an analysis of the moist Kelvin wave. J Atmos Sci 45:2051–2065

Wang B, Li T (1994) Convective interaction with boundary-layer dynamics in the development of a tropical intraseasonal system. J Atmos Sci 51:1386–1400

Wang B, Rui H (1990) Synoptic climatology of transient tropical intraseasonal convection anomalies: 1975–1985. Meteorol Atmos Phys 44:43–61

Wang B, Wu R, Li T (2003) Atmosphere-warm ocean interaction and its impacts on Asian-Australian monsoon variation. J Clim 16:1195–1211

Wang B, Webster P, Kikuchi K, Yasunari T, Qi Y (2006) Boreal summer quasi-monthly oscillation in the global tropics. Clim Dyn 27:661–675

Wang L, Li T, Zhou T (2012) Intraseasonal SST variability and air-sea interaction over the Kuroshio Extension region during boreal summer. J Clim 25:1619–1634

Wang L, Li T, Zhou T, Rong X (2013) Origin of the intraseasonal variability over the North Pacific in boreal summer. J Clim 26:1211–1229

Wen M, Yang S, Higgins W, Zhang R (2011) Characteristics of the dominant modes of atmospheric quasi-biweekly oscillation over tropical-subtropical Americas. J Clim 24:3956–3970

Wheeler MC, Hendon HH (2004) An all-season real-time multivariate MJO index: development of an index for monitoring and prediction. Mon Weather Rev 132:1917–1932

Xu Y, Li T, Peng M (2014) Roles of the synoptic-scale wave train, the intraseasonal oscillation, and high-frequency eddies in the genesis of typhoon Manyi (2001). J Atmos Sci 71:3706–3722

Yanai M, Esbensen S, Chu JH (1973) Determination of bulk properties of tropical cloud clusters from large-scale heat and moisture budgets. J Atmos Sci 30:611–627

Yang J, Wang B, Wang B, Bao Q (2010) Biweekly and 21–30-day variations of the subtropical summer monsoon rainfall over the lower reach of the Yangtze River basin. J Clim 23:1146–1159

Yang S, Wu B, Zhang R, Zhou S (2013a) Relationship between an abrupt drought-flood transition over mid-low reaches of the Yangtze River in 2011 and the intraseasonal oscillation over mid-high latitudes of East Asia. Acta Meteorol Sinica 27:129–143

Yang S, Wu B, Zhang R, Zhou S (2013b) The zonal propagating characteristics of low-frequency oscillation over the Eurasian mid-high latitude in boreal summer. Sci China Earth Sci 56:1566–1575

Yokoi S, Satomura T (2006) Mechanisms of the northward movement of submonthly scale vortices over the Bay of Bengal during the boreal summer. Mon Weather Rev 134:2251–2265

Zhang C (2005) Madden–Julian oscillation. Rev Geophys 43:RG2003. doi:10.1029/2004RG000158

Zhang Y, Li T, Wang B, Wu G (2002) Onset of the summer monsoon over the Indochina Peninsula: climatology and interannual variations. J Clim 15:3206–3221

Zhao C, Li T, Zhou T (2013) Precursor signals and processes associated with MJO initiation over the tropical Indian Ocean. J Clim 26:291–307

Zhou L, Sobel AH, Murtugudde R (2012) Kinetic energy budget for the Madden–Julian oscillation in a multiscale framework. J Clim 25:5386–5403